The Interstellar Medium at High Redshift: The Sub-DLA at z=2.06 Towards the Quasar J2123−0050

by

Nikola Milutinović

University of Victoria

The Interstellar Medium at High Redshift: The Sub-DLA at z=2.06 Towards the Quasar J2123−0050

by

Nikola Milutinović
B.Sc., The Pennsylvania State University, 2005

A Thesis submitted in Partial Fulfillment of the
Requirements for the Degree of

Master of Science

in the

Department of Physics and Astronomy

Supervisory Committee

The Interstellar Medium at High Redshift: The Sub−DLA at z=2.06 Towards the Quasar J2123−0050

by

Nikola Milutinović
B.Sc., The Pennsylvania State University, 2005

Supervisory Committee

Dr. S. Ellison, (Department of Physics and Astronomy)

Supervisor

Dr. D. Vandenberg, (Department of Physics and Astronomy)

Departmental Member

Dr. L. Simard, (Department of Physics and Astronomy, NRC/HIA)

Departmental Member

Supervisory Committee

Dr. S. Ellison, (Department of Physics and Astronomy)
Supervisor

Dr. D. Vandenberg, (Department of Physics and Astronomy)
Departmental Member

Dr. L. Simard, (Department of Physics and Astronomy, NRC/HIA)
Departmental Member

Abstract

DLAs are the primary reservoirs of neutral gas available for star formation at high redshift. However, DLAs are metal poor and lack molecular gas. In this thesis, I present a study of an extraordinary case of a z=2.06 sub-DLA towards the quasar J2123−0050, which is characterized by a metallicity that approaches solar, and a high H_2 molecular fraction ($\log f(H_2) = -2.54$). Furthermore, this SDLA harbors HD molecules, only the third such detection at high redshift, and with the highest ($HD/2H_2$) fraction of −2.75. To understand these observations, I study the effects of dust depletion and photoionization on the interpretation of raw abundance measurements. I find that the magnitude of photoionization and dust depletion effects has a profound impact on the interpretation of this SDLA. The calculated corrections lower the elemental and molecular abundances suggesting that the ISM in the SDLA towards J2123−0050 exhibits properties similar to the gas in the local sightlines.

Table of Contents

List of Tables

List of Figures

Chapter 1 | *Introduction*

Recent breakthroughs in observational technology, achieved with 10m class telescopes and space-based observatories, have given us the opportunity to look deep into the cosmos. A magnificent amount of new data unravelled with these instruments has allowed us to push the horizons of our knowledge pertaining to the nature of the world that surrounds us. Cosmic Microwave Background (CMB) radiation experiments (such as The Wilkinson Microwave Anisotropy Probe – *WMAP*) have probed the epochs just after the universe became optically thin, allowing a vast sea of photons to fill up the universe. This echo of the Big Bang gives us valuable information on the state of matter when the universe was only about 400,000 yr old. What directly follows from the CMB observations is that the early universe was homogeneous to a very high degree. In fact, inhomogeneities of the matter density were only on the order of one in a thousand. Everything that exists today hails from these tiny primordial fluctuations at the beginning of the time. Gravitation allowed these small over-densities to grow so that most of the matter density clustered in density peaks over cosmic time. This resulted in the emergence of a network of overdense filaments, sheets, knots, and underdense voids that lie in between – the conglomerate that is often dubbed the "cosmic web" (Bond, Kofman, & Pogosyan 1996).

Advances in computational technology have provided an opportunity to model the universe as it evolved from the primordial density fluctuations to the large scale structure that we observe in redshift surveys of galaxies today (such as Sloan or the 2dFGRS). Figure 1.1 shows the large scale structure in Sloan, 2dFGRS, and CfA2 galaxy catalogues in comparison with the dark matter halos extracted from the

Millennium simulation by Springel et al. (2005). Both the data and the simulations point to a picture in which halos merge through the cosmic time to form larger structures. This hierarchical clustering scenario is currently the popular theory of cosmic structure growth. In the current scenario, the first stars light up some time beyond a redshift of 10 when the gas within the haloes having virial temperatures on the order of 10^4 K cooled rapidly through Lyα and H_2 emission (Madau (2007), and references therein). These first (Pop III) stars synthesized heavy elements and dispersed them into the immediate environment after exploding as supernovae. This gas again cools down and is then funneled through the filaments to knots where it forms proto-galaxies. These early galactic structures are usually beyond the scope of our current direct observational ability, but indirect observations — for example through Quasar Absorption Lines (QAL) — have been of great scientific importance for understanding the cosmic web, and galactic formation and evolution.

1.1 Quasar Absorption Lines

Quasars are extremely luminous, high-redshift objects associated with active galactic nuclei. Their luminosities often vary on the timescale of the order of weeks, days, or even hours that constrain their relatively small size (e.g. a quasar with a one week luminosity variation can be, at most, one light week across). The high emission output from such a small spatial size requires a very efficient energy source. It is most likely that gravitational energy release from a matter falling onto the central black hole acts as an engine for the radiation. The typical spectrum of a quasar is presented in Figure 1.2. The spectrum shows a non-thermal continuum coming from an optically thick accretion disk heated by the supermassive black hole. The Lyα emission from neutral hydrogen, as well as the metal line emission, is superimposed on the continuum. These emission lines are often kinematically broad and arise from the high-speed gas that is highly irradiated by the quasar

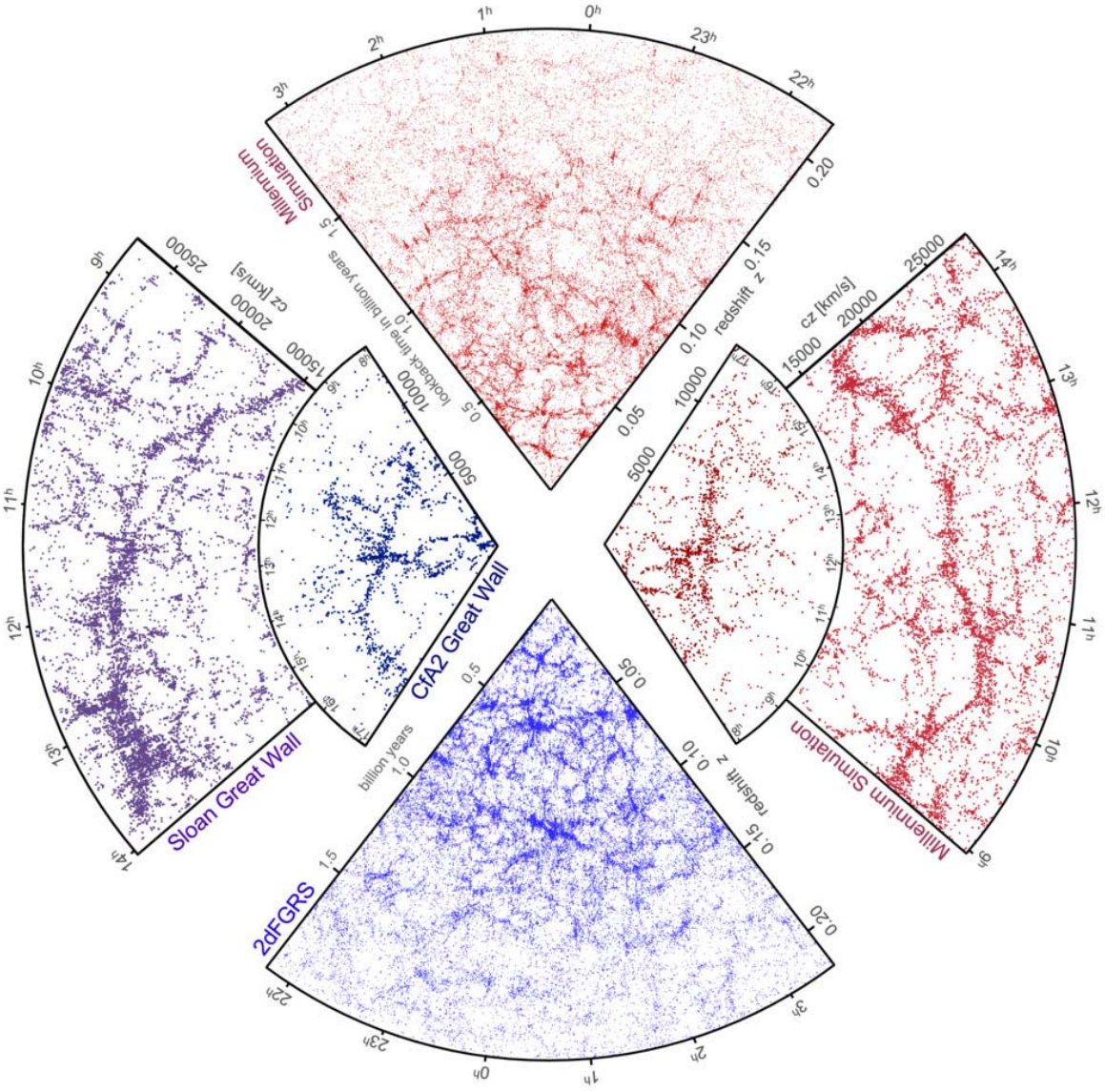

Figure 1.1: Large scale structure in Sloan, CfA2 and 2dFGRS galaxy catalogues compared to Millennium simulation. The data show filaments mapped with overdensities of galaxies, and underdense voids. Figure is reproduced from Springel, Frenk, & White (2006)

producing a wide range of ionization stages. The quasar spectrum also shows a multitude of absorption lines, some of which arise from gas intrinsic to the quasar (associated systems), while others come from intervening gas along the line of sight between the observer and the quasar. As the photons traveling of the quasar towards the observer intersect the network of filaments, sheets and knots in the cosmic web, they get absorbed leaving a signature in the quasar spectrum as shown in Figure 1.2. The most prominent lines are due to the absorption of neutral hydrogen through the Lyman series lines blueward from the quasar's Lyα emission (with the Lyα line being the strongest in the series) . Metal lines are also present in a variety of ionization stages from neutral to highly ionized species.

1.1.1 QAL Systems

The discovery of absorption lines in quasar spectra came in the mid sixties following the work of Sandage (1965) and Gunn & Peterson (1965). At first, the cosmological origin of the absorption was highly contested and it was proposed that these absorption lines arose from the gas associated with the quasar itself. However, the extremely large velocities that absorbing cloudlets would need to have in order for this hypothesis to be supported, as well as consistency of absorption distribution functions from quasar to quasar left no doubt that these systems are produced by gas clouds along the line of sight (Bahcall & Salpeter 1965). Soon after, high resolution spectra became available that allowed in-depth studies of quasar absorption lines. A classification scheme has been developed in which metal-line absorbers are attributed to interstellar gas in intervening galaxies, whereas the Lyα forest (a collective name for Lyα absorption blueward of the Lyα emission) was thought to be primordial gas residing in the inter-galactic medium (Sargent et al. 1980; Weymann, Carswell & Smith 1981). However, with the development of larger telescopes in the last two decades, it became clear that even the Lyα forest is not free of metals. A large fraction of absorbers with N(HI)$> 10^{15}$ cm^{-2} have

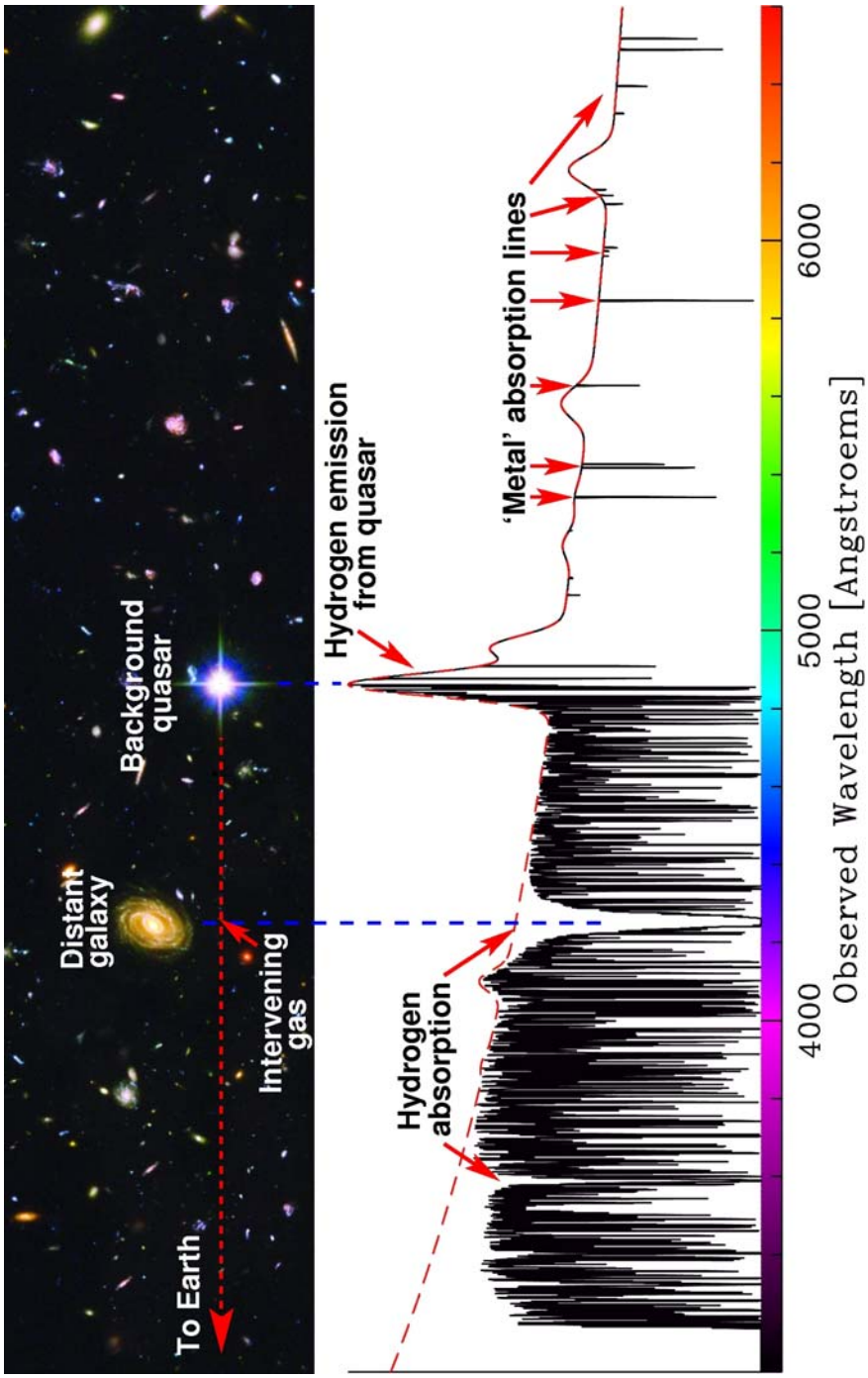

Figure 1.2: A simulated quasar spectrum showing the non-thermal continuum, emission from the associated gas, as well as a plethora of absorption lines. The figure is courtesy of John Webb.

Table 1.1: Summary of QAL systems and their column density classifications.

System type	log N(H I)	Spectral signature	Usually associated with	References
Ly α forest	$\lesssim 17.5$	Ly α $\lambda_0 = 1215.67$ Å	IGM	Rauch (1998)
			weak MgII systems	Steidel (1995),
				Churchill & Charlton (1999),
				Milutinovic et al. (2007)
Lyman limit systems	$\gtrsim 17.5$	912 Å break	Galactic Halo	Tytler (1982),
			Strong Mg II systems	Lanzetta et al (1995)
Damped Ly α systems	$\gtrsim 20.3$	Ly α $\lambda_0 = 1215.67$ Å	Proto-galaxy	Wolfe (1988),
				Lanzetta et al (1995)
				Wolfe et al (2005)

associated metal lines, such as CIV, and OVI doublets (Cowie et al. 1995, Tripp et al. 2008) and weak MgII doublet lines (Narayannan et al. 2005; Milutinović et al. 2006).

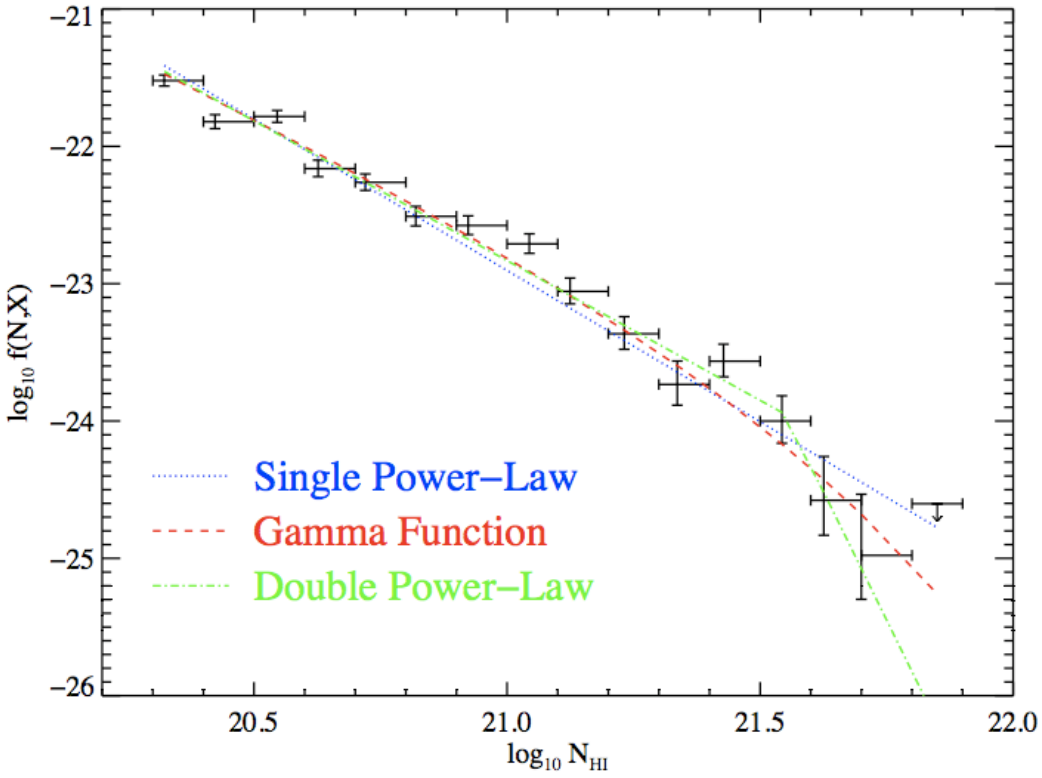

Figure 1.3: The N(HI) frequency distribution for QALs. A single power law provides a good fits to the data, except in the highest density regime. The other two functions presented on the plot (Gamma function, and double power law) present the more acceptable fits to the data. Plot taken from Prochaska et al. (2005)

The quasar absorption line systems are traditionally named by the transition which primarily identifies them. However, all the metal systems have associated neutral hydrogen absorption, and it is usual to classify the systems based on the strength of HI. Table 1.1 gives the classification scheme along with the typical neutral hydrogen column densities. While the division between Lyα forest and Lyman Limit Systems (LLSs) is set by the absence or presence of the 912 Å break

due to the absorption in neutral hydrogen, Damped Lyα Systems, or DLAs have characteristic damping wings in their Lyα profiles.

The column density distribution of QAL systems is presented in Figure 1.3. Most of the distribution is well fitted by a single power law $A \times N(\mathrm{H\,I})^{\beta}$ (with an index of $\beta \sim -1.5$), which breaks down only in the case of the highest column density absorbers. This means that the majority of absorbers have low neutral hydrogen column densities, but the total $N(\mathrm{H\,I})$ in the universe is dominated by high column density absorbers.

1.1.2 Damped Lyα Absorbing Systems

DLAs are traditionally defined as absorbers with a column density of neutral hydrogen of $N(\mathrm{H\,I}) \geq 2 \times 10^{20}$ cm^{-2}. This definition has its rationale in the fact that the absorbers with this column density of H I are mostly neutral. The definition is also partly historical, hailing from the observational limitations of the first survey of Wolfe et al. (1986) whose spectra had a FWHM of only 10 Å and could therefore reliably pick out only the highest density absorbers (with $\log N(\mathrm{H\,I}) \geq 20.3$ cm^{-2}). At the time, it was already known from 21 cm maps of local spiral galaxies that the column density drops from 10^{21} at galactic centres to 2×10^{20} cm^{-2} at 1.5 Holmberg radii ($R_{26.5}$) in disks (Wolfe, Gawiser, & Prochaska 2005). The survey was constructed with the goal of detecting disk galaxies, which were expected to be in place at high redshift in pre-ΛCDM scenarios.

Due to their high column density, DLAs are relatively rare compared to other QAL systems. At z$>$ 2, on average, one out of three sightlines to a high-z QSO contains a DLA. Even though they are rare, due to the small exponent ($\beta \sim -1.5$) of the power law that describes the QAL column density distribution, these highest column density absorbers dominate the total mass density of neutral hydrogen, $\Omega_{DLA} \approx \Omega_{\mathrm{H\,I}}$, at high-z. At z$\sim$3 the mass density of DLAs takes a value of $\Omega_{DLA} \sim 3 \times 10^{-3}$. Since the mass density of luminous matter in nearby spiral galaxies was

thought to have a similar value about a decade ago (see Lanzetta et al. 1991), this led to speculations that DLAs contain sufficient gas mass to account for all present day stars (Wolfe 1987; Lanzetta et al. 1991; Lanzetta et al. 1995). This bestowed DLAs as powerful instruments in the study of gas consumption into stars over cosmic time (Storrie-Lombardi & Wolfe 2000). However, the present estimate of stellar mass density, $\Omega_\star$, exceeds Ω_{DLA} at high-z by more than a factor of two. This means that the closed box gas-to-stars model for DLAs is unlikely to be correct. Furthermore, the reservoir of neutral gas needs to be replenished before the current epoch. However, DLAs still do contribute a significant fraction of the gas available for star formation at z>1.6.

There have been attempts to directly measure the star formation rate (SFR) density in DLAs through Lyα emission. This method gives a lower limit on the SFR due to the extreme sensitivity of Lyα photons to dust. In the handful of DLAs sampled with this method, Wolfe et al. (2003) suggest that SFRs in DLAs are comparable to those in Lyman break galaxies. A more indirect method, using CII* absorption was proposed by Wolfe, Prochaska & Gawiser (2003). In Wolfe et al. (2008), the authors apply this model to a sample of 76 DLA. Assuming that the gas is in the cold neutral phase, they calculate the SFR density of DLAs in their sample to be $10^{-3.2}\leq\Sigma_{SFR}(M_\odot yr^{-1}kpc^{-2})\leq10^{-1.2}$. They also find that DLAs exhibit bimodality in their CII* column density SFR density distribution. Moreover, these two subsamples had distinct distributions of velocity width, metal abundance, and dust-to-gas ratio. However, the HI column density was consistent with being drawn from a single distribution. Wolfe et al. (2008) conclude that one of these populations has *in situ* star formation that is heating the gas, while the other is likely to be heated by some close FUV radiation source (e.g., a compact bulge of a Lyman break galaxy). These results support the hypothesis that DLAs are indeed closely connected to star forming regions in the high-z universe.

However, this simple scenario is not without caveats. DLAs are mostly metal

poor and lack molecular hydrogen, which is unexpected if they trace the regions of star formation. The average metallicity of a DLA is only [M/H]~ -1.2. Herbert-Fort et al. (2006) performed a comprehensive metallicity study of more than 1000 DLA systems found in the SDSS database in order to search for more enriched ones. They find that absorbers with $N(\mathrm{Zn}^+) \geq 10^{13.5}$ or $N(\mathrm{Si}^+) \geq 10^{15.95}$, which they define as metal-strong DLAs, constitute only about $\sim$5% of the total population at redshift greater than 2.2. Extensive abundance studies (see, for example, the USCD/Keck abundance database of 153 DLAs at z>1.6 analyzed by Prochaska et al. 2007) agree that DLAs are metal poor at all redshifts, but also find a metallicity floor at [M/H]≈ -2.6 (Wolfe et al. 2005). The metallicity in DLAs also exhibit a very slow evolution from high-redshifts towards the present epoch with a slope of -0.18 ± 0.12 dex z^{-1} (Péroux et al. 2003). However, the mean DLA metallicity does not reach the solar value even at $z = 0$ as may be expected if they dominate gas in star-forming galaxies. The total mass density of metals observed in DLAs and LBGs is also roughly a factor of 5 below what is expected from the cosmic star formation history (Pettini 1999). This "missing metals problem" has been a hot topic in QAL astrophysics in recent years, with authors proposing that significant amounts of metals might be hidden in different phases, like a very hot, collisionally ionized medium (Ferrara et al. 2005), or is ejected into the IGM via outflows from small galaxies (Bouché et al. 2007).

While molecular gas is ubiquitous throughout the Galaxy, Ledoux, Petitjean & Srianand (2003) report the detection of molecular hydrogen in only 15% of the DLAs in their sample. The H_2 content of these absorbers is also lower by three orders of magnitude compared to the average Galactic H_2 fraction [$f(H_2) = N(H_2)/(N(\mathrm{H\,I})+N(\mathrm{H\,II})+2N(H_2)) \sim 10^{-1}$], but is similar to that found in the Magellanic Clouds. Remarkably, $\sim$ 75% of the Ledoux DLA sample have H_2 fractions on the order of 10^{-6}. This low rate of molecule detection is likely connected with the low metallicities or enhanced radiation fields in DLAs. For example, Petitjean

et al. (2006) studied a sample of metal rich DLAs and concluded that metallicity is indeed an important criterion for the presence of molecular gas in DLAs. This does not come as a surprise given the level of the correlation between the dust depletion and metallicity (Ledoux et al. 2003), and knowing that the presence of dust is crucial for H_2 formation.

1.1.3 Sub Damped Lyα Absorbing Systems

Much attention in recent years has been turned to a new sub-class of the QAL systems called Sub Damped Lyα systems, or SDLAs. SDLAs are a sub-class of LLSs whose Lyα profile does exhibit the presence of damping wings, but their column densities are too small to classify them as DLAs ($10^{19} \leq N(\mathrm{H\,I})_{SDLA} < 2 \times 10^{20}$ cm^{-2}). These systems outnumber DLAs by approximately a factor of 4 and could contribute to a significant fraction of the cosmic metal mass (Prochaska et al. 2006), and gas available for star formation. In fact, Péroux et al. (2003) postulate that at z>3.5 these systems contribute about 45% of the neutral gas mass. The slope of the metallicity evolution for SDLAs is slightly more pronounced than for DLAs (-0.40 ± 0.22 dex z^{-1}) (Péroux et al. 2003). However, these results depend heavily on the few sightlines at the low redshift, while the DLAs and SDLAs seem to follow the same evolution at higher redshifts (Dessauges-Zavadsky, Ellison, & Murphy 2009). The observational effort of Péroux et al. (2007) provided an upper limit to the contribution of SDLAs to the metal mass budget, accounting to only about $\sim 6\%$. Even though SDLAs are mostly ionized (Wolfe, Gawiser, & Prochaska 2005), there are at least a couple of H_2 detections in SDLAs (Ledoux, Petitjean, & Srianand 2003, Srianand et al. 2008). Furthermore, the SDLA at $z = 2.418$ towards SDSSJ143912.04+111740.5 is the only high-z QAL system with detected CO and HD absorption along with H_2 (Srianand et al. 2008). This discovery highlights the importance of studying SDLAs for our understanding of high-z ISM.

Abundance measurements, and metallicity estimates in SDLAs are highly affected by the presence of an ionized phase since these absorbers have lower HI column densities compared to those in DLAs. Many authors have attempted to produce models to estimate the levels of photoionization in these systems (Dessauges-Zavadsky et al. 2003, Prochaska et al. 2002, Vladilo et al. 2001) but they generally disagree on the level of the ionization corrections and their implications for the global metallicity contribution and the general importance of SDLAs. This controversy motivated the case study of the remarkable SDLA towards J2123−0050 that is presented in this thesis.

1.2 The Absorption Lines Theory

In order to introduce the QAL research field terminology used in the thesis a brief review of the basics of absorption line theory is given below.

1.2.1 The Voigt Profile

The profile of an absorption line is governed by both the physical properties of the absorbing cloud and the atomic properties of the absorbing species. The optical depth, τ_λ takes the shape of the Voigt profile:

$$\tau_\lambda = N\alpha(\lambda) = N\alpha_{natural}(\lambda) \otimes g(\Delta\lambda), \tag{1.1}$$

where N is the column density and α is the absorption coefficient given as a convolution of the Lorentzian natural absorption coefficient per atom $[\alpha_{natural}(\lambda)]$ and the normalized Gaussian probability distribution of atoms $[g(\Delta\lambda)]$. The convolution of a Lorentzian and a Gaussian is the Voigt function, u, so the optical depth can be

written as:

$$\tau_\lambda = N\frac{\pi e^2\lambda_r^2}{m_e c^2} f u(x,y) \quad \text{where} \quad u(x,y) = \frac{1}{\pi^{1/2}\Delta\lambda_D} H(x,y), \tag{1.2}$$

where f is the oscillator strength, $\Delta\lambda_D$ the Doppler width, and H(x,y) the Hjerting function of the form:

$$H(x,y) = \frac{y}{\pi}\int_{-\infty}^{+\infty} \frac{\exp(-t^2)}{(x-t)^2+y^2} dt, \tag{1.3}$$

with

$$x = \frac{\Delta\lambda}{\Delta\lambda_D} \quad \text{and} \quad y = \frac{\Gamma\lambda_r^2}{4\pi c}\frac{1}{\Delta\lambda_D}. \tag{1.4}$$

In this equation x is an independent variable that is simply the difference between the wavelength along the profile and the line center in units of the Doppler width.

The observed absorption profile is given with the function:

$$I(\lambda) = I^0(\lambda)\exp(-\tau(\lambda)), \tag{1.5}$$

where $I(\lambda)$, and $I^0(\lambda)$ are the observed flux and continuum at wavelength λ.

The Doppler widths are usually written in the terms of b-parameter, which is defined as:

$$b^2 = b_{therm}^2 + b_{turb}^2, \tag{1.6}$$

where b_{turb} is a turbulent broadening component, and b_{therm} is the thermal component, which can be further written as:

$$b_{therm} = \frac{c}{\lambda}\Delta\lambda_D = \left(\frac{2kT}{m}\right)^{1/2}. \tag{1.7}$$

The expression for the optical depth at the line core then follows from Equation 1.2:

$$\tau(\lambda_0) = 1.497\times 10^{-15}\frac{N(\mathrm{cm}^{-2}) f \lambda_0(\mathring{A})}{b(\mathrm{km\,s}^{-1})} \tag{1.8}$$

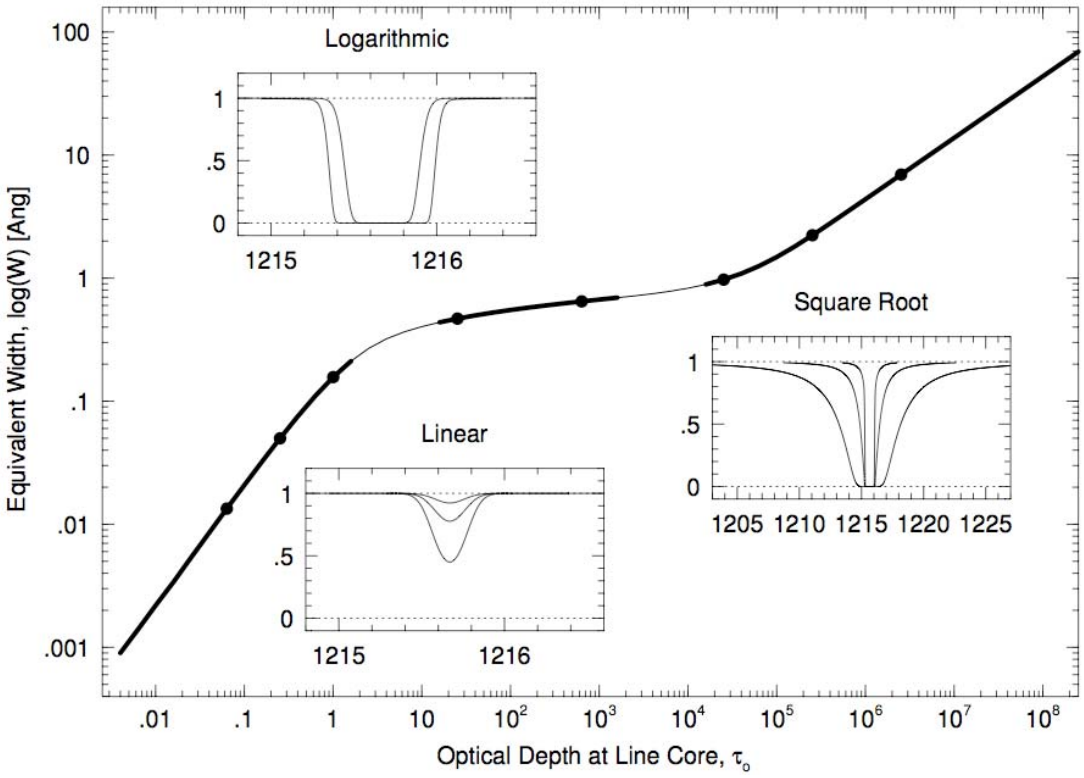

Figure 1.4: A curve of growth showing the equivalent width as a function of the optical depth at the line core for aLyα line with $b = 30$ km s^{-1}. The three regimes are represented by the thick curves along with the typical absorption profiles for varying column density. The Figure is reproduced from (Churchill 2009, in prep).

1.2.2 The Curve Of Growth

While the most powerful technique to fit the spectral features is Voigt profile fitting, for unresolved lines one can turn to a curve of growth analysis which relies on the measurement of the equivalent width. The equivalent width is given by:

$$W = \int_{-\infty}^{+\infty} \left(1 - \frac{I(\lambda)}{I^0(\lambda)}\right)\, d\lambda = \int_{-\infty}^{+\infty} (1 - \exp(-\tau(\lambda)))\, d\lambda. \tag{1.9}$$

Equation 1.9 means that the equivalent width is a function of optical depth, which is itself a function of the b-parameter, and the column density and it defines the so called curve of growth (COG). The COG depends on the strength of the absorption line which is defined by the three regimes shown in Figure 1.4, the linear, the logarithmic and square root regime.

In the linear regime of the curve of growth the line is unsaturated and is characterized by a small column density, which can be calculated as:

$$N(\mathrm{cm}^{-2}) = 1.13 \times 10^{20} \frac{W}{\lambda_0^2 f}. \tag{1.10}$$

In the the linear regime, the column density is linearly proportional to the equivalent width and does not depend on the b-parameter. As the column density increases, the line saturates and transitions to the logarithmic portion of the curve. In this regime, the equivalent width depends on both the b-parameter and the column density through the expression:

$$N(\mathrm{cm}^{-2}) = \frac{2b\lambda_0}{c} \sqrt{\ln\left(\frac{\sqrt{\pi} e^2 N \lambda_0 f}{m_e c b}\right)}. \tag{1.11}$$

Voigt profile fitting is very uncertain in this regime because the strong b-parameter dependence causes a degeneracy between the optical depth and the column density. As the column density of the gas increases (at $N \gtrsim 10^{19}$ cm^{-2} for Lyα) the Lorentzian component in the profile starts dominating, which manifests itself by the emergence of damping wings. This regime is called the square root regime and

is given by the expression:

$$N(\mathrm{cm}^{-2}) \sim \frac{\sqrt[3/2]{\lambda_0}}{c}\sqrt{\left(\frac{e^2 N \lambda_0 f \Gamma}{m_e c}\right)}, \tag{1.12}$$

where Γ is the damping constant.

Chapter 2 | *Data*

DLAs and SDLAs give rise to a plethora of strong absorption features from neutral hydrogen in the rest-frame UV, as well as in the radio band of the electromagnetic spectrum due to the hyperfine transition of neutral hydrogen at 21 cm. While the 21 cm detections are valuable because they allow for the measurement of hyperfine spin temperature, they tell us nothing about the associated metal and molecular absorption at the incident redshift. Furthermore, the fraction of radio-loud quasars is quite low, which leaves us with a relatively small number of systems that can be studied using this technique. On the other hand, along with neutral hydrogen absorption, the UV and optical regimes host a multitude of metal and molecular line transitions. The abundance of strong features makes it possible to study Lyα absorption through the use of rather low resolution (FWHM$\sim$ 10 Å) spectra with moderate signal-to-noise ratios, as in the first surveys for DLAs (e.g., the Lick Survey of Wolfe et al. (1986)). However, in order to probe the coldest absorption phase and to perform detailed studies of the associated metal lines that are often as narrow as a couple of $\mathrm{km\,s^{-1}}$, one needs to obtain spectra of significantly higher resolution.

2.1 Instrumentation

The High Resolution Echelle Spectrograph (HIRES) mounted on the Keck I telescope (Vogt et al. 1994) was used to obtain the data presented in this thesis. HIRES is a standard in-plane echelle spectrograph with grating cross-dispersion, permanently mounted at a Nasmyth focus of Keck I. The design with two collima-

tors, sensitive at blue (HIRESb) and red (HIRESr) wavelengths, provides a coverage in the spectral range from $\sim 3,000$ Å up to $\sim 11,000$ Å. The light path through HIRES is shown in Figure 2.1.

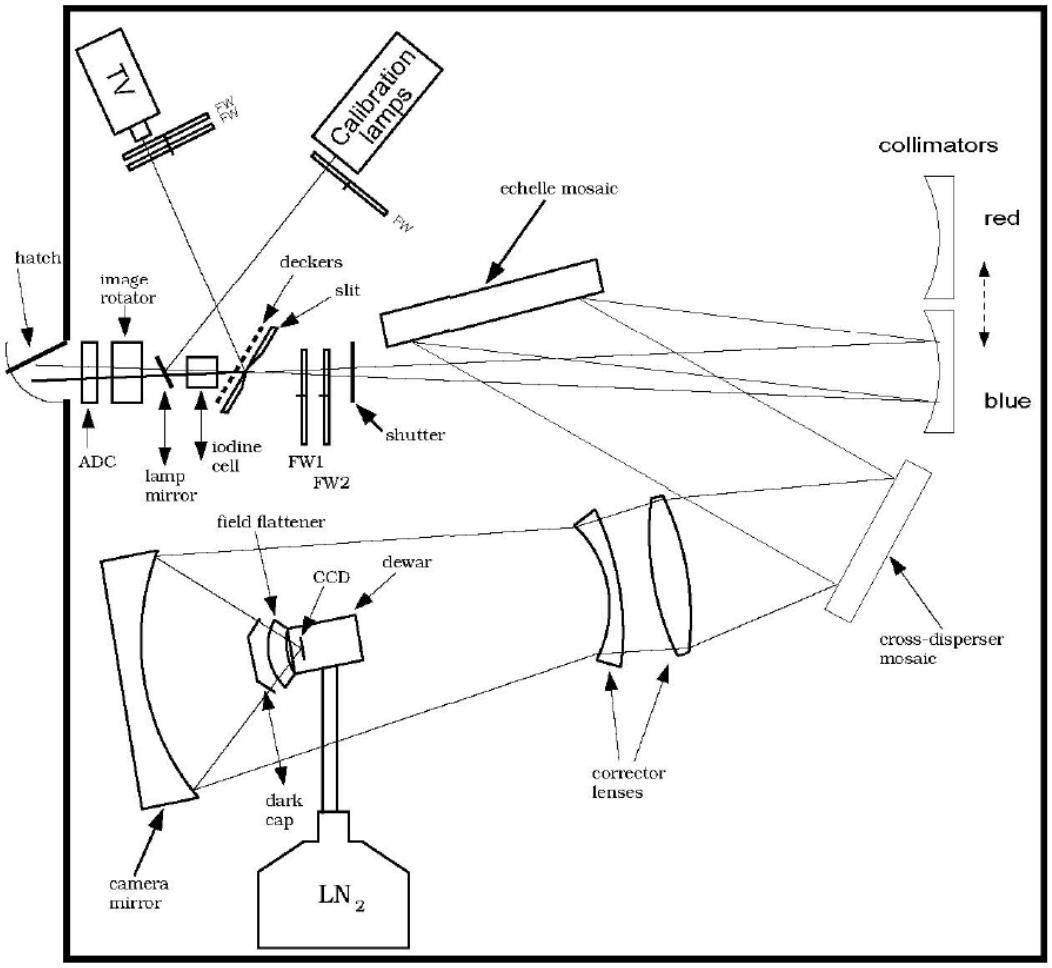

Figure 2.1: Light-path schematics of HIRES. Image reproduced from the HIRES manual (Vogt et al. 1994).

The light enters the instrument at the f/13.7 Nasmyth focus and falls onto the image rotator that is used to control the position angle of the slit on the sky. The observer can opt for a parallactic angle orientation in which the slit is normal to the horizon. In this position, the atmospheric refraction varies along the length of the slit. The slit size (both length and width) is regulated by a set of deckers

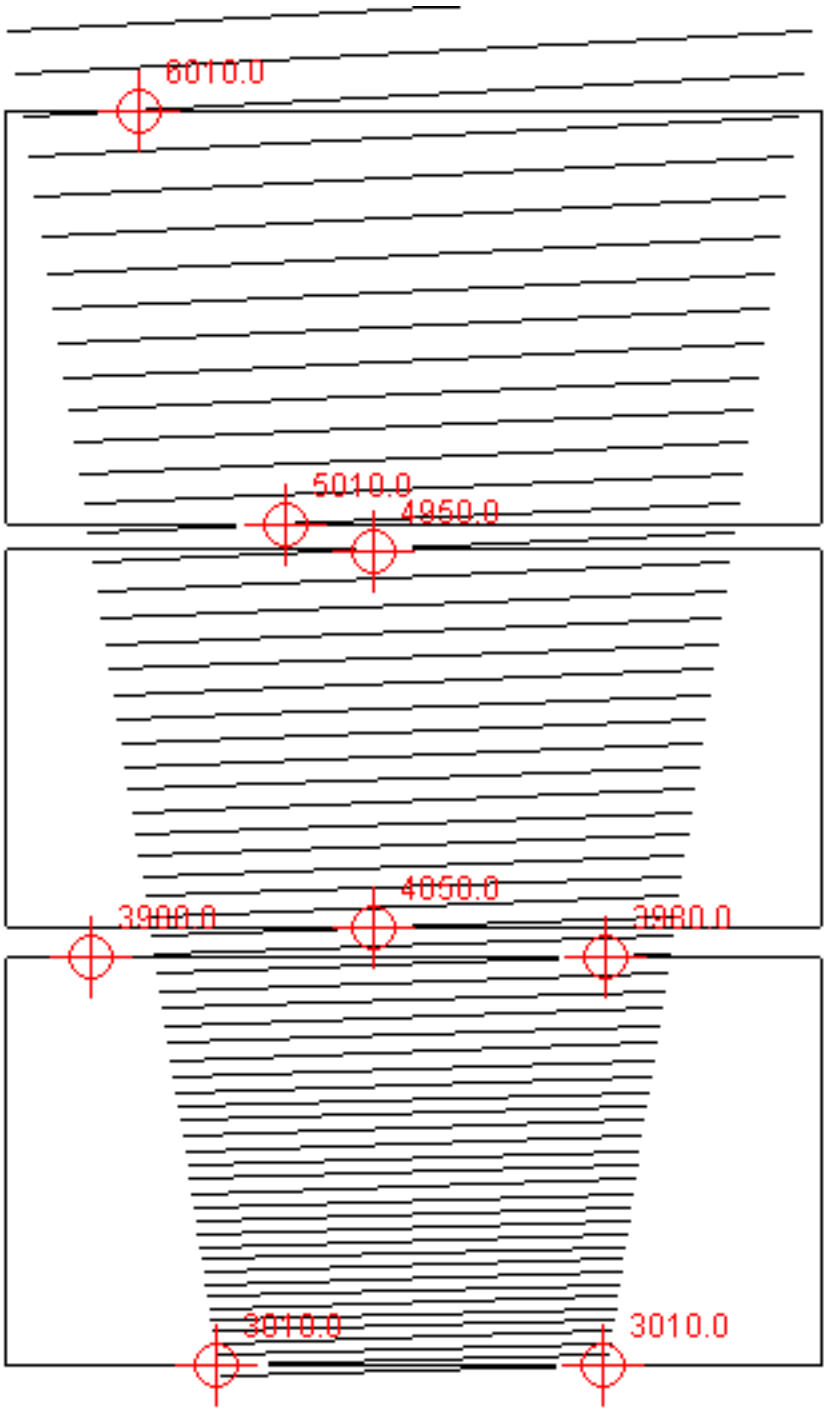

Figure 2.2: The simulated image of HIRES echellogram using the blue collimator, and echelle and cross-disperser angles of 0° and 1.°025 respectively. Circles show the approximate positions of different wavelengths projected on the 3 CCD mosaic.

(there is also the option of using a classical slit, but this is more or less obsolete due to the large choice of deckers available). The slit plane is tilted so that the light can be reflected up to the TV camera which provides a continuous view of the target. This feature is especially useful when guiding on very faint targets, as is typical of quasars. After the filter wheel and the shutter, light arrives at one of the two available collimators. Both are physically identical, except that the blue one has a two layer dielectric aluminium coating which allows for high throughput from 0.3 to 0.5 μm, while the red one has an enhanced silver coating which is efficient in reflecting the light in the 0.34 to 1.1 μm range. The beam is reflected from the collimator to the mosaic of 3 echelles each 12″ by 48″ in size. The ruling of the grating is 52.68 grooves mm^{-1}, and the blaze angle is 70.5°. The cross-disperser is a mosaic of two 12″ by 16″ gratings ruled with 250 grooves mm^{-1}, and is intended to be used in 1st order for visible (blaze peak near 0.56 μm), and 2nd order in ultraviolet light (blaze peak at 0.28 μm). Finally, through a set of corrective lenses the light goes into the camera. Optically, the camera is an all spherical polychromatic f/1 system. The detector set consists of a mosaic of three 2k x 4k MIT/Lincoln Labs CCDs with a pixel size of 15 μm. Even though the detectors are highly efficient, this set–up has the disadvantage of not allowing for continuous coverage of the whole spectral range since some orders will always fall in the gaps between the detectors. The observer can adjust the positioning of the echelle orders' image on the camera's focal plane by changing the echelle and cross-disperser angles, thus controlling which part of the spectrum will be lost to the gaps (see the Figure 2.2 for the simulated image of a Keck/HIRES echelleogram).

2.2 Data Acquisition and Reduction

The optical spectrum of J2123−0050 that is analyzed in this thesis was obtained as a part of the pilot-sample program for the search for molecular hydrogen in DLAs.

Motivated by the results of Tumlinson et al. (2002) our team (consisting of S. Ellison, J. X. Prochaska (JXP), J. Tumlinson and myself) designed an experiment to search for molecular hydrogen in the metal-strong subsample of the Sloan Digital Sky Survey (SDSS) DLAs DR5 (Herbert-Fort et al. 2006). For all the high redshift quasars ($z > 1.6$) and $r < 19.5$ in SDSS DR5 database we ran an automated search for absorption in 14 resonance lines (such as SiII λ1808, FeII λ2600 and OI λ1302). From ∼20,000 quasars searched, Herbert-Fort et al. (2006) found more than 2,000 metal absorption systems, which were graded according to their line strength. Approximately 150 systems are found to have very strong metal lines, some of which include the detections of weak transitions (e.g. ZnII λ2026) that usually require a 10 m class telescope and echelle spectrograph for detection. In $> 95\%$ of these cases where Lyα is also covered in the SDSS spectrum, it was found that the HI column density is large, and the absorber would be classified as a DLA. Follow-up observations of a sub-sample of these metal-line selected DLAs with HIRES have shown that the metallicities of these DLAs are approaching the solar value, even at z∼2 (Herbert-Fort et al. 2006). The metal strong DLAs represent promising candidates for follow-up searches for molecular hydrogen, since previous H_2 surveys indicate a higher detection rate for high metallicity DLAs (Petitjean et al. 2006). The absorber at z=2.035 towards J2123−0050 was selected as a candidate for an H_2 absorption bearing system because of the strong absorption in SiII λ1808 in the SDSS spectrum (Figure 2.3).

The SDLA towards J2123−0050 was first discovered in optical wavelengths in the SDSS at a right ascension of 21h 23′ 29.″46, and a declination of −00° 50′ 52.″90. It is a relatively bright quasar with a magnitude of r=16.44. The Lyα emission from the quasar is centred at a redshift of z_{qso}=2.26. The NRAO VLA Sky Survey reported a radio loud object within ∼20 arcsec of the SDSS position (Condon et al. 1998). The first high resolution optical observation of this target was performed

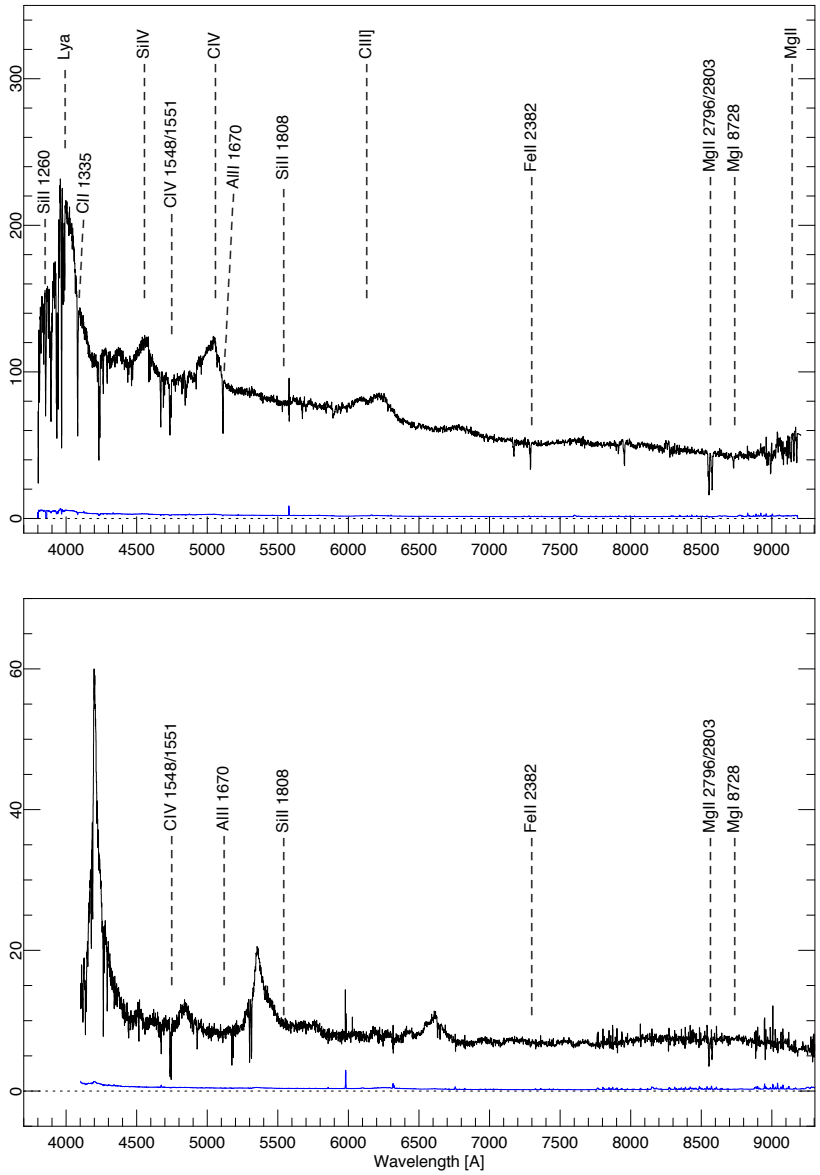

Figure 2.3: The SDSS spectrum of J2123−0050 (upper panel) compared with the spectrum of J0751+3533 (lower panel) which contains a low metallicity DLA with $[\alpha/\mathrm{H}] \approx -2.6$. The spectrum of J0751+3533 is redshifted so that the position of the DLA aligns with the SDLA towards J2123−0050. One can notice that the lower panel spectrum lacks the detection of some of the marked lines, which are detected in the upper one. The presence of these lines is suggestive of high metallicity.

by JXP with Keck/HIRES as a part of our Canadian Gemini exchange 2006B allocation time. On August 18th, 2006 we performed the first observations of the target with the C1 decker (0.86 arcsec wide), yielding a resolution of R∼45,000. After the preliminary reduction analysis at the telescope showed the detection of H_2, we decided to obtain follow-up observations with the decker E3 (0.4 arceses wide) that would result in a spectral resolution of R∼100,000. The high resolution is beneficial when studying the coldest phases of the extra-galactic ISM, allowing to resolve often very narrow components of the diffuse gas (for more details consult Narayanan et al. 2006).

On July 19, 2006, starting at 9:37:55 UT, J. X. Prochaska repeated the observations of the target using the 0.″4 wide E3 decker (giving a FWHM resolution of ∼3km s^{-1}), echelle angle of 0°, and cross-disperser angle of 1.°0275 for three exposures of 3,600 sec each, for a total of 3 h (see Figure 2.2 for the simulated image of the echelleogram with these settings). The sky conditions were typical for Mauna Kea, with a seeing of 0.″72, varying up to 1.″1 throughout the exposures. For calibration purposes, the observer obtained a set of standard trace flats, as well as the spectra of ThAr lamps (arcs) using the same instrument settings. The calibration frames were taken at the beginning and the end of the observing night, as well as prior to the science exposures. Along with this, we also obtained a set of pixel flats (lamp flats) at the beginning of the observing run to determine the pixel-to-pixel variation across the detectors. These were taken prior to the first night of observing since it is safe to assume that the detector's pixel response is stable at least over the course of a few days.

The data were reduced (by me) using the HIRedux routine, written by JXP, which is a part of the xIDL package*. HIRedux can be used in both an automatic and manual mode. In order to monitor the reduction process I ran the pipeline in manual, step-by-step mode. The reduction involved the following procedures:

*xIDL is publicly available at http://www.ucolick.org/∼xavier/IDL/index.html

- A combined pixel flat is produced from a stack of about 30 pixel flat exposures for each of the detector's chips. These are used to correct small pixel-to-pixel variations over the chips.

- In a similar manner, a combined trace flat frame is produced as a median over the series of standard flat images taken during the observing night. This frame is then used to define (trace) the echelle order boundaries (and find the order of curvature), and to determine the slit profile, which is used to correct the illumination pattern of the science frames. Both of these steps ensure optimal sky subtraction and object extraction in the science frames.

- A wavelength calibration is derived from the spectra of ThAr lamp taken with the same setup used for the science frames. HIRedux processes arc images in a significantly different manner from the standard procedure for echelle spectrographs. Rather than mapping a ThAr spectrum onto a linear wavelength scale, the pipeline performs a 1D wavelength solution by fitting the low-order Legendre polynomials to the pixel values versus the laboratory wavelengths along the spatial centres of each order. After that, the code performs a 2D fit to all the lines from the 1D solution. Finally, the pipe-line derives the 2D wavelength map giving both the wavelength solution, and the line tilts for all orders over the full echelle footprint. This type of reduction is absolutely crucial when working in the high resolution mode where the FWHM is on the order of only a couple of km s^{-1}.

- After the raw science frame images are flattened and cosmic rays are flagged, the final step in the reduction process is the extraction of the objects and the sky subtraction. The pipeline does this procedure in the standard manner – the code automatically identifies and traces the object in each order. This gives a trace solution as a function of wavelength and echelle order number. The sky background is estimated from the pixels that fall well beyond the

object aperture, taking into account diffuse scattered light, which is estimated by interpolating the pixel counts in the gaps between the pixel orders. After this the procedure derives the spatial profile of the object PSF, and performs the optimal extraction. The end result is a 2D spectrum of flux and sigma for each echelle order, and each of the exposures.

- Finally, all three exposures were coadded by combining each order separately. This maximizes the signal-to-noise, which is important for the orders whose edges have relatively low signal (especially in the blue).

The fluxing of echelle spectra is a fairly difficult task. However, since we are only interested in measurements of equivalent widths (column densities) and kinematic properties of the absorption lines in the normalized spectrum, this task is not necessary for this study, and was not performed. The final 1D spectrum is obtained after the separate normalization of each order. The continuum is fitted manually using the xIDL routine *x_continuum*. The routine allows the user to select the parts of continuum unaffected by the absorption and then performs a minimum χ^2 fit on the selected data points using a spline function of a given order (for the HIRES data presented here the usual value of the spline order is around 8). The echelle orders are finally averaged into a 1D spectrum weighted by the square of the median signal-to-noise ratio. The final spectrum spans from $\sim$ 3000 Å to $\sim$ 6000 Å, and has a S/N of $\sim$ 15 per pixel at 3100 Å, $\sim$ 30 at 3500 Å, and $\sim$ 40 at 5100 Å. A representative sample of normalized data is presented in Table 2.1 and Figure 2.4[†].

2.3 Measurements

In order to measure the column densities of absorbing species and determine elemental abundances, there are several standard techniques, which are commonly

[†]The spectrum is publicly available at http://www.astro.uvic.ca/∼milni/H2/J2123−0050.fits

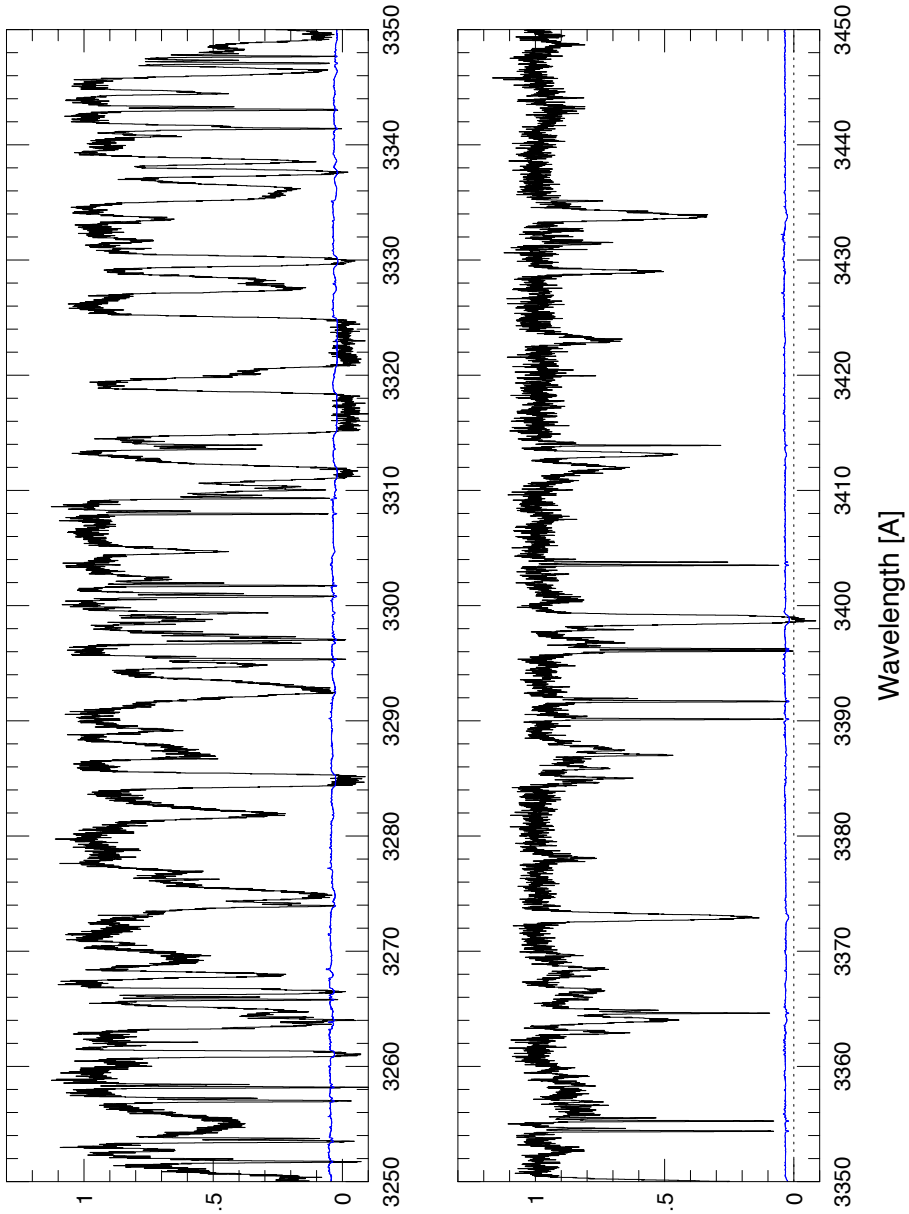

Figure 2.4: A representative section of Keck/HIRES J2123−0050 normalized spectrum.

Table 2.1: Sample of the data from the normalized Keck/HIRES J2123−0050 Spectrum

$\lambda_r[\AA]$	flux	sigma	$\lambda_r[\AA]$	flux	sigma
...			3850.2139	1.00532	0.02221
3850.0302	1.00792	0.02228	3850.2306	0.99916	0.02219
3850.0469	1.02668	0.02222	3850.2473	1.01260	0.02227
3850.0636	1.01067	0.02224	3850.2640	0.95752	0.02181
3850.0803	0.97925	0.02208	3850.2807	1.01871	0.02230
3850.0970	0.95718	0.02182	3850.2974	0.97241	0.02197
3850.1137	0.93720	0.02161	3850.3141	0.95962	0.02185
3850.1304	0.94061	0.02160	3850.3307	0.97643	0.02189
3850.1471	0.91711	0.02148	3850.3474	0.98790	0.02216
3850.1638	0.93361	0.02167	3850.3641	1.00431	0.02226
3850.1805	0.94080	0.02180	3850.3808	0.98397	0.02209
3850.1972	0.99194	0.02193	....		

used in QAL research practice: Voigt profile fitting, apparent optical depth measurements, and the curve of growth method. High resolution spectroscopy makes it possible to resolve the absorption lines, and allows for the decomposition of line blends. Voigt profile fitting is generally regarded as the optimum fitting procedure. However, in the case of complex kinematic absorption structure, saturated lines, and heavy blending, it is practical to approach the measurements on a case-by-case basis.

The J2123−0050 spectrum shows absorption from the Lyman series lines with a damped Lyα profile. To perform the column density measurement of such a broad, damped line, and to minimize the influence of continuum fitting on the Voigt fit, I chose to simultaneously fit the continuum and the line profile to a blaze-normalized chunk of the spectrum, encompassing the Lyα absorption. I performed the fit using the x_fitdla routine of XIDL. The Lyα profile is ~ 500 km s^{-1} wide at its base, and is

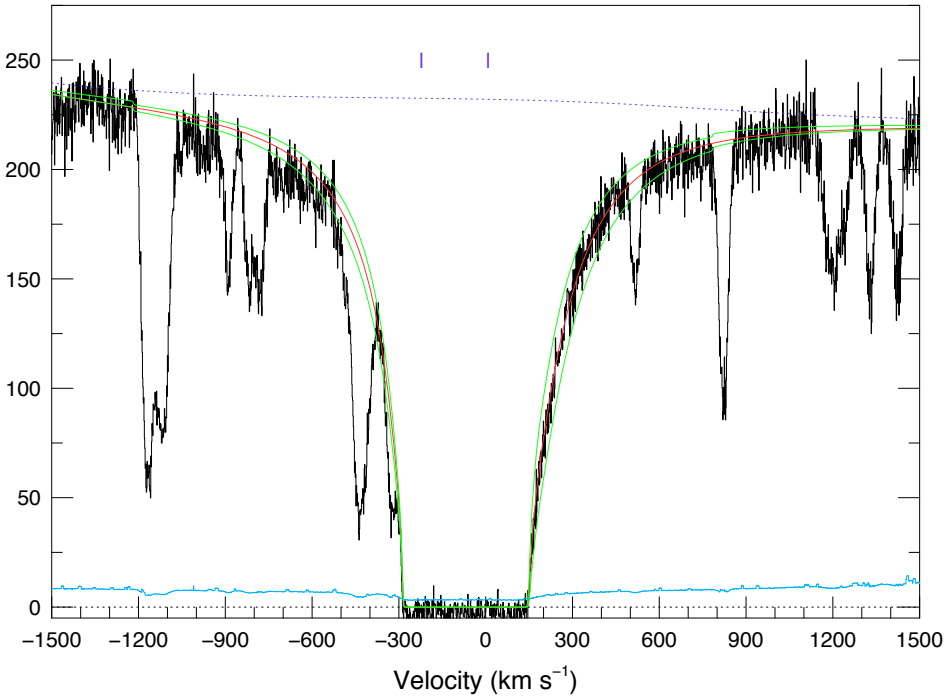

Figure 2.5: Fit to Lyα [log$N$(H I) = 19.18±0.15 cm^{-2}]. The HIRESb data is flattened out with the blaze function prior to fitting. The blue line represents the continuum fit, while the red and green lines are the line profile and 3σ bands respectively. A two component fit is required to adequately fit the asymmetric profile. The column densities of separate components are log$N$(HI z = 2.0593)=19.18±0.15 cm^{-2}, and log$N$(HI z = 2.05684)=18.40±0.30 cm^{-2}.

asymmetric, with the red wing showing stronger damping. The assymetry indicated that a two-component fit was necessary. The redshifts of components were fixed at the redshifts of the strongest metal line absorption in the two kinematically distinct metal line complexes detected in the system (see the further description of the complexes in the Chapter 4). The fit is presented in Figure 2.5. The total column density of hydrogen is log$N$(H I)= 19.25±0.2 cm^{-2}, while the column densities of the

separate components are log$N$(HI $z = 2.0593$)=19.18±0.15 cm^{-2}, and log$N$(HI $z =$ 2.05684)=18.40±0.30 cm^{-2}. This fitting approach is not physically motivated, since it is likely that the absorption is arising from many kinematically narrower cloudlets along the line of sight. Nevertheless, this method gives a good estimate of both the total neutral hydrogen column density, and the column density of separate absorption complexes that correspond to the structure seen in the metal lines.

Along with the neutral hydrogen, the absorber at z≈2.059 gives rise to a kinematically complex system of absorption in many metal species. In order to derive the total column density of multi-component metal line complexes I employed the strategy of minimizing the number of components with VPFIT 9.3 (Carswell et al. 1996) over the normalized data. VPFIT is a multiple Voigt profile fitting code that calculates a maximum likelihood fitting function to the data. The code is adapted to fit multiple lines simultaneously, which allows for efficient identification of blends. The goodness of fit is assessed in VPFIT by χ^2 statistics. The error estimates of the fitting parameters also include the uncertainties induced by self-blends, as well as blends due to unidentified lines. In cases in which no unsaturated lines are measured for an ion, I report the result of the fit as a lower limit. For a non-detection, a 3σ upper limit to the column density is calculated using the following set of equations:

$$W_{obs(3\ \sigma)} = 3 \times FWHM/(S:N), \tag{2.1}$$

$$W_r = W_{obs}/(1+z), \tag{2.2}$$

$$N = 1.13e20 \times W_r/(\lambda_r \times f), \tag{2.3}$$

where W_r, and λ_r are rest-frame equivalent width and wavelength, f is the oscillator strength, and $(S:N)$ is the signal to noise ratio at the observed line wavelength.

I start the fitting by selecting the transitions with the visually clearest kinematic structure, with little, or no, blends, and no saturation. I fit these lines separately using the interactive fit mode in VPFIT. This serves as a database of initial guesses

Table 2.2: Neutral Carbon and Silicon Column Densities from Voigt Profile Fits

z	b (km s^{-1})	log N(CI) (cm^{-2})	log N(CI*) (cm^{-2})	log N(CI**) (cm^{-2})	log N(SI) (cm^{-2})
2.05933	1.83±0.30	13.73±0.02	13.42±0.03	12.43±0.02	12.08±0.05
2.05957	7.25±4.00	12.91±0.03	12.74±0.10	12.16±0.11	...
Total		13.79±0.02	13.50±0.03	12.62±0.03	12.08±0.05

Table 2.3: Limits To Metal Ion Column Densities

log N(CII) (cm^{-2})	log N(NII) (cm^{-2})	log N(OI) (cm^{-2})	log N(ArI) (cm^{-2})	log N(NiII) (cm^{-2})	log N(AlII) (cm^{-2})
≥ 15.2	≥ 12.0	≥ 15.7	≥ 12.2	$\leq$11.66	≥ 13.51

for the fitting process. Initial input for VPFIT was obtained by tying the redshifts and b-parameters of a certain velocity component in all the metal species to the metal with the visually clearest, unsaturated component at the incident redshift. I let the code reduce the number of velocity components by minimizing the χ^2 of the fit. The results of the fit are presented in Tables 2.2 through 2.5, as well as in Figures 2.6 and 2.7. While this fitting method produces a good estimate of the total column density, it does not necessarily yield a unique solution to the structure of individual absorbing clouds. Specifically, the presented absorption components might be a blend of two or more clouds that occupy a narrow kinematic space. This is not of concern for us because we are mostly interested in the total column densities of the SDLA. However, it was necessary to separate the fits into the neutral (Table 2.2), singly ionized (Table 2.4), and highly ionized gas phases (Table 2.5), since a single fit to all phases had a high χ^2 and did not produce satisfactory results.

We also detected molecular transitions of hydrogen from both Lyman and Werner bands up to rotational level $J = 5$. The absorption arises in two kinematically distinct components, at the velocity of the strongest metal complex. The H_2 lines are

Table 2.4: Metal Ions Column Densities from Voigt Profile Fits

z	b (km s^{-1})	log N(SiII) (cm^{-2})	log N(FeII) (cm^{-2})	log N(NiII) (cm^{-2})	log N(AlII) (cm^{-2})	log N(AlIII) (cm^{-2})	log N(SII) (cm^{-2})	log N(NI) (cm^{-2})	log N(CII) (cm^{-2})	log N(CII*) (cm^{-2})
2.05684	5.24 ± 0.20	13.43 ± 0.02	12.93 ± 0.06	...	...	11.86 ± 0.04	...	...	...	...
2.05698	3.90 ± 0.24	13.20 ± 0.02	12.62 ± 0.09	...	...	12.05 ± 0.03	...	...	...	...
2.05714	4.47 ± 0.20	13.28 ± 0.02	12.72 ± 0.08	...	...	11.74 ± 0.05	...	...	...	...
2.05743	3.86 ± 0.28	13.03 ± 0.02	12.74 ± 0.07	...	...	10.85 ± 0.37	...	...	...	...
2.05800	6.24 ± 1.48	12.46 ± 0.08	...	...	...	10.81 ± 0.44	...	...	...	...
2.05836	8.46 ± 1.26	12.71 ± 0.05	12.14 ± 0.32	...	...	11.39 ± 0.14	...	...	...	...
2.05880	7.29 ± 0.82	12.90 ± 0.04	12.75 ± 0.08	...	...	11.65 ± 0.07	...	...	...	...
2.05896	3.98 ± 0.19	13.35 ± 0.02	12.74 ± 0.06	...	...	11.89 ± 0.04	...	...	...	...
2.05919	5.15 ± 0.23	13.57 ± 0.03	12.74 ± 0.05	...	...	12.13 ± 0.03	13.72 ± 0.06	13.38 ± 0.04	...	12.55 ± 0.07
2.05930	4.84 ± 0.12	14.18 ± 0.06	13.18 ± 0.07	...	...	11.86 ± 0.07	14.16 ± 0.04	14.34 ± 0.02	...	13.35 ± 0.03
2.05943	11.32 ± 0.87	14.11 ± 0.06	13.43 ± 0.07	...	...	12.73 ± 0.02	14.07 ± 0.07	...	...	12.78 ± 0.16
2.05955	6.44 ± 0.22	13.82 ± 0.05	13.24 ± 0.05	...	...	12.06 ± 0.04	14.20 ± 0.03	14.00 ± 0.02	...	13.19 ± 0.03
2.05979	10.10 ± 0.47	13.45 ± 0.02	13.40 ± 0.04	...	...	11.79 ± 0.06	...	...	...	12.62 ± 0.06
2.06017	5.02 ± 0.23	13.68 ± 0.02	13.49 ± 0.02	...	...	11.92 ± 0.04	13.43 ± 0.10	...	...	...
2.06047	6.46 ± 2.06	12.40 ± 0.11	...	...	...	...	...	...	...	...
Total		14.69±0.02	14.12±0.02	≤ 11.66	≥ 13.51	13.06 ± 0.04	14.70±0.02	14.53±0.02	≥ 15.2	13.71±0.01

Table 2.5: CIV and SiIV Column Densities from Voigt Profile Fits

z	b (km s^{-1})	log N(CIV) (cm^{-2})	log N(SiIV) (cm^{-2})
2.05685	8.97 ± 0.54	13.32 ± 0.08	12.70 ± 0.07
2.05695	6.56 ± 3.21	13.21 ± 0.73	12.07 ± 1.05
2.05698	4.09 ± 0.44	13.18 ± 0.45	13.00 ± 0.09
2.05704	4.02 ± 1.24	13.15 ± 0.32	12.47 ± 0.30
2.05711	4.72 ± 0.89	13.05 ± 0.15	12.68 ± 0.11
2.05721	7.48 ± 0.90	13.04 ± 0.06	12.34 ± 0.07
2.05749	19.50 ± 1.59	13.12 ± 0.03	12.39 ± 0.04
2.05800	18.70 ± 1.02	13.21 ± 0.02	12.40 ± 0.03
2.05838	13.45 ± 2.24	12.60 ± 0.11	12.01 ± 0.10
2.05879	6.30 ± 0.39	12.75 ± 0.03	12.22 ± 0.04
2.05916	55.37 ± 11.75	13.48 ± 0.17	12.68 ± 0.14
2.05923	6.55 ± 0.19	13.83 ± 0.05	13.30 ± 0.04
2.05930	8.84 ± 1.23	13.96 ± 0.18	13.38 ± 0.23
2.05943	28.59 ± 7.37	13.50 ± 0.10	12.88 ± 0.13
2.05947	12.82 ± 3.78	13.68 ± 0.34	13.23 ± 0.32
2.05978	12.10 ± 1.90	12.95 ± 0.16	12.37 ± 0.12
2.06018	6.34 ± 1.18	11.78 ± 0.29	11.83 ± 0.07
2.06033	28.40 ± 3.23	13.08 ± 0.07	11.96 ± 0.13
Total		14.48 ± 0.01	13.86 ± 0.01

located at the same redshifts as the neutral lines of carbon, which aligned with the strongest singly ionized metal ion lines.

The stronger component is saturated for most of the rovibrational transitions up to J=3, so I developed a curve of growth (COG) routine in IDL in order to recover the column densities of separate J-states. First, I carefully visually selected the lines that are not affected by blends, and measure their equivalent widths by fitting the multi-component Voigt profiles with the software FITTER, which has been kindly provided to us by C.W. Churchill. The software gives the decomposed values

Table 2.6: H_2 Column Densities

rot level	z = 2.05930		z = 2.05957	
	b (km s^{-1})	log N (cm^{-2})	b (km s^{-1})	log N (cm^{-2})
J= 0	4.60±0.34	15.70±0.08	6.37±0.56	14.15±0.05
J= 1	4.60±0.29	16.20±0.13	6.37±0.28	14.87±0.03
J= 2	4.60±0.24	15.40±0.06	6.37±0.22	14.50±0.01
J= 3	4.60±0.35	15.35±0.07	6.37±0.67	14.58±0.05
J= 4	4.60±1.70	14.25±0.13	6.37±2.15	13.63±0.11
J= 5	–	≤13.80	–	–
Total per cloud		16.32±0.03		15.21±0.01
Total		16.34±0.03		

of equivalent widths component-by-component. I used these values to minimize the χ^2 of the COG. The fitting routine makes use of molecular data of Abgrall, Roueff, & Drira (2000) and assumes the same b-parameter for all of the states. For each 0.025 km s^{-1} step in b, the code inter-loops through the column densities of rotational levels (starting at level J=0) producing a single COG for all the states. This procedure allows the column densities of the J-states with saturated lines to be recovered. The results are given in Figure 2.10. The total column density of H_2 is obtained from VPFIT by forcing the COG derived values to the stronger component, and fitting the weaker, unsaturated component using the same strategy as for the metal lines. Since all the transitions to the rotational level $J = 5$ are affected by blends, I quote only an upper limit to the column density in this case, although the impact of $J = 5$ states on the total column density of H_2 is likely to be minimal. The final fits are presented in Figure 2.8. The total column density of H_2 is $\log N(H_2) = 16.34 \pm 0.03$ cm^{-2}. Table 2.6 lists the values for individual components and J-states.

Along with H_2, we detect HD transitions in the ground rotational state aligned in

Table 2.7: HD Molecule. The detected transitions and their oscillator strengths.

Transition	$\lambda_r[\AA]$	f
HD B5-0R(0)	1036.545	2.684e-02
HD B0-0R(0)	1108.127	1.665e-03
HD B3-0R(0)	1062.882	1.790e-02
HD B2-0R(0)	1076.992	1.144e-02
HD B7-0R(0)	1012.810	2.970e-02
HD B8-0R(0)	1001.821	2.677e-02

velocity with the strongest H_2 component. This is only the third reported detection of the HD molecule in the high-redshift universe (see also (Varshalovich et al. 2001) and (Srianand et al. 2008)). The singly deuterated hydrogen molecule is detected only in a few transitions in the ground state in both the Lyman and Werner bands, listed in Table 2.7, along with the newly measured HD oscillator strengths from Ivanov et al. (2008). The transition from vibrational state 5 to 0 (B5-0R(0)) is the only line unaffected by blends. From the VPFIT to this line I obtained a column density of $\log N(\mathrm{HD}) = 13.89 \pm 0.04$ cm^{-2} and a b-parameter of $b = 2.68 \pm 0.34$ km s^{-1}. The fits are presented in Figure 2.9.

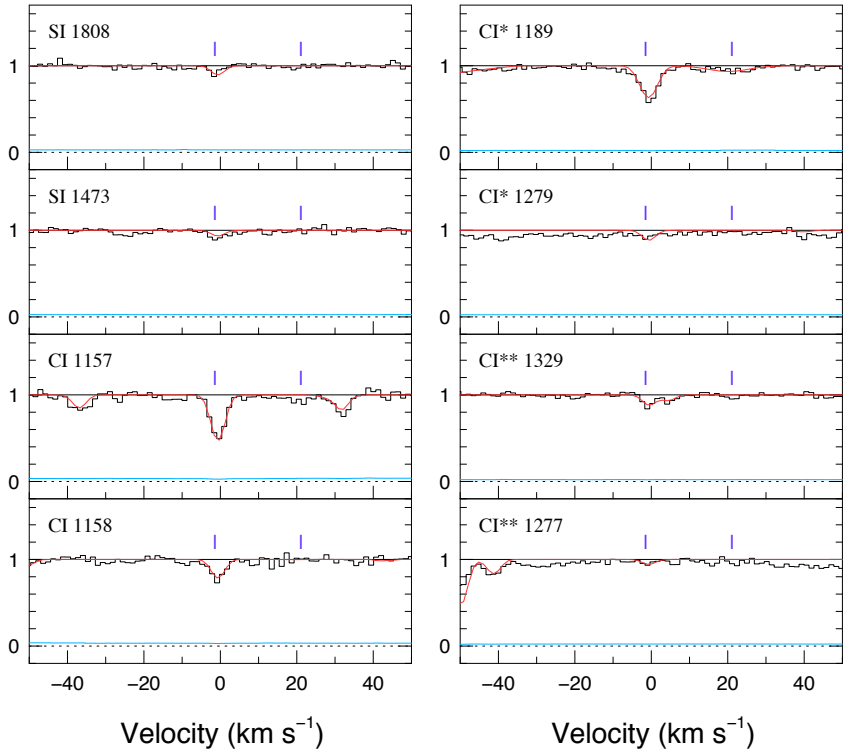

Figure 2.6: Fits to neutral carbon and sulphur lines towards J2123−0050 on a velocity scale relative to $z = 2.05930$. The vertical thick marks indicate the position of the velocity components which give rise to molecular absorption. The data is presented in black, the error arrays are given in blue, while the fits are red line.

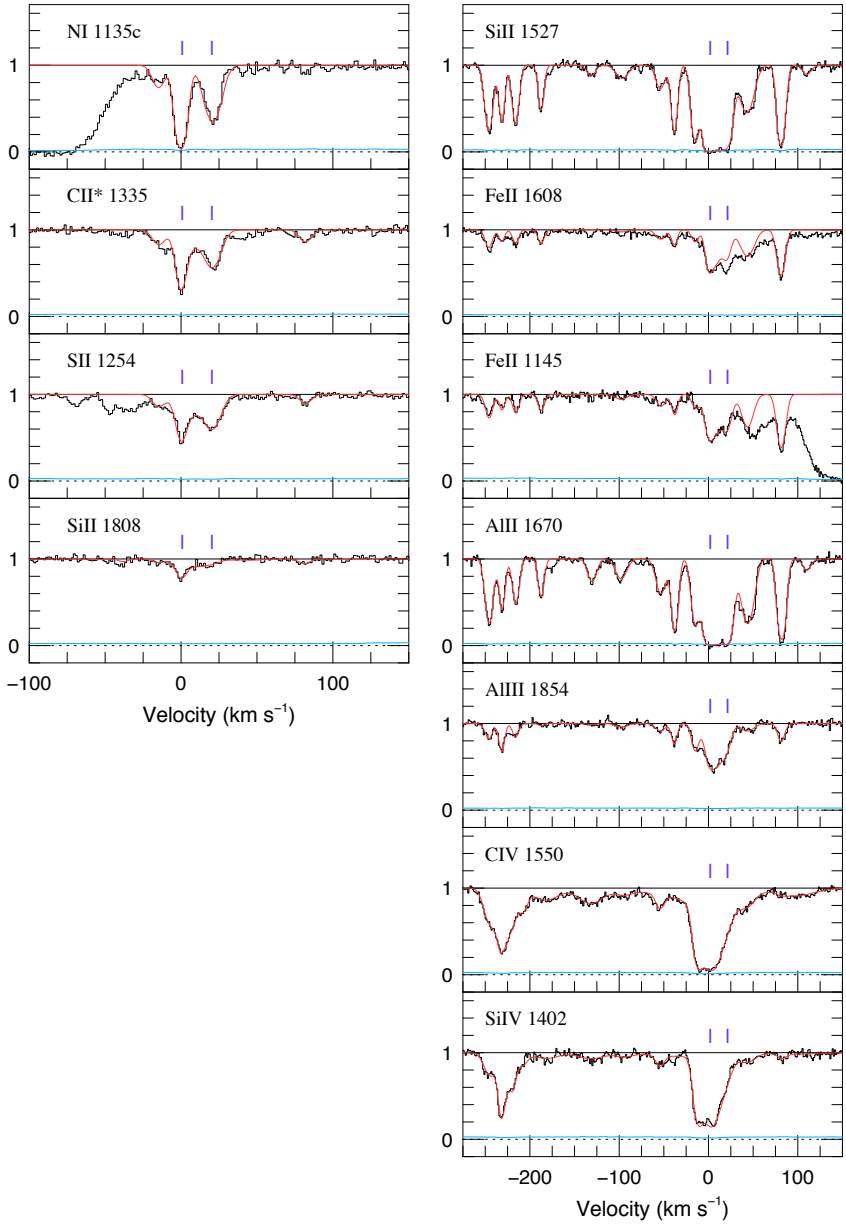

Figure 2.7: Fits to metal lines towards J2123−0050 on a velocity scale relative to $z = 2.05930$.

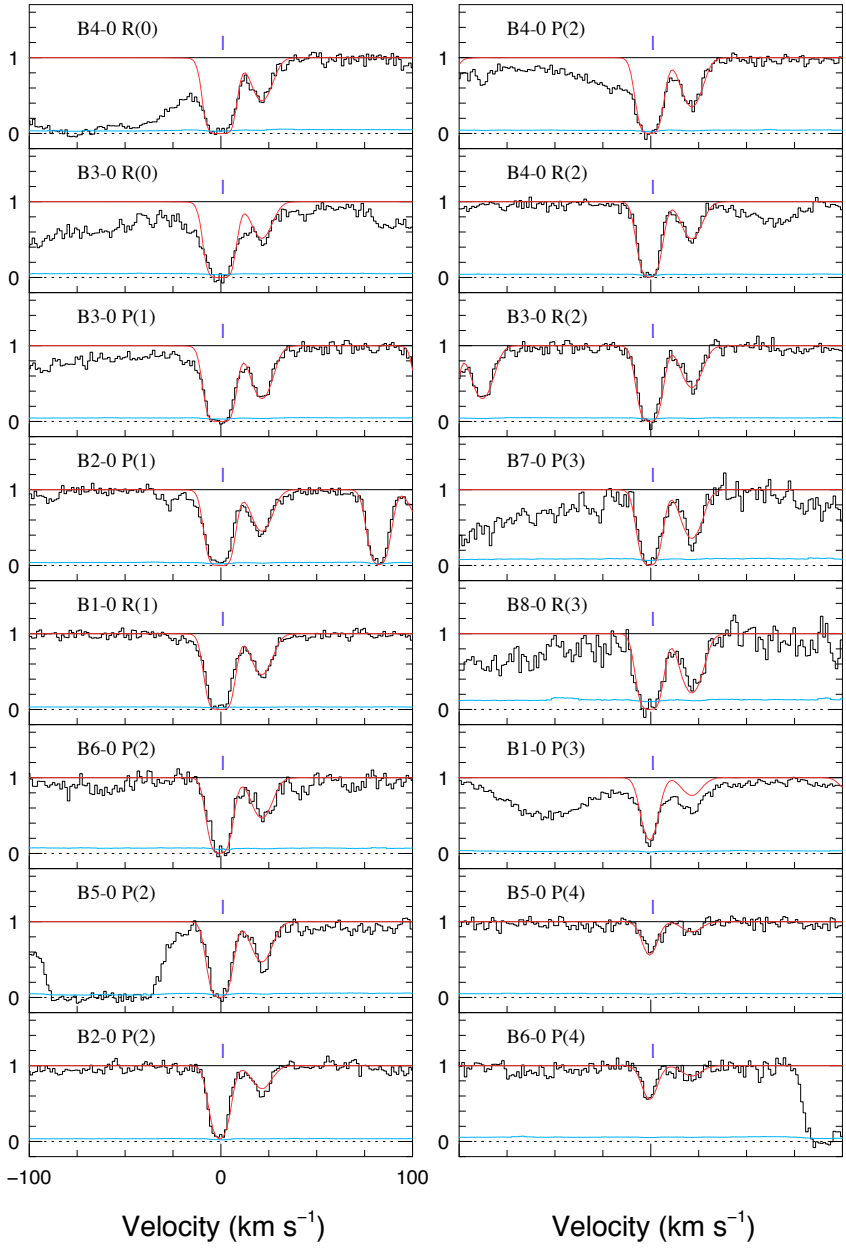

Figure 2.8: Fits to molecular Hydrogen lines towards J2123−0050 on a velocity scale relative to $z = 2.05930$.

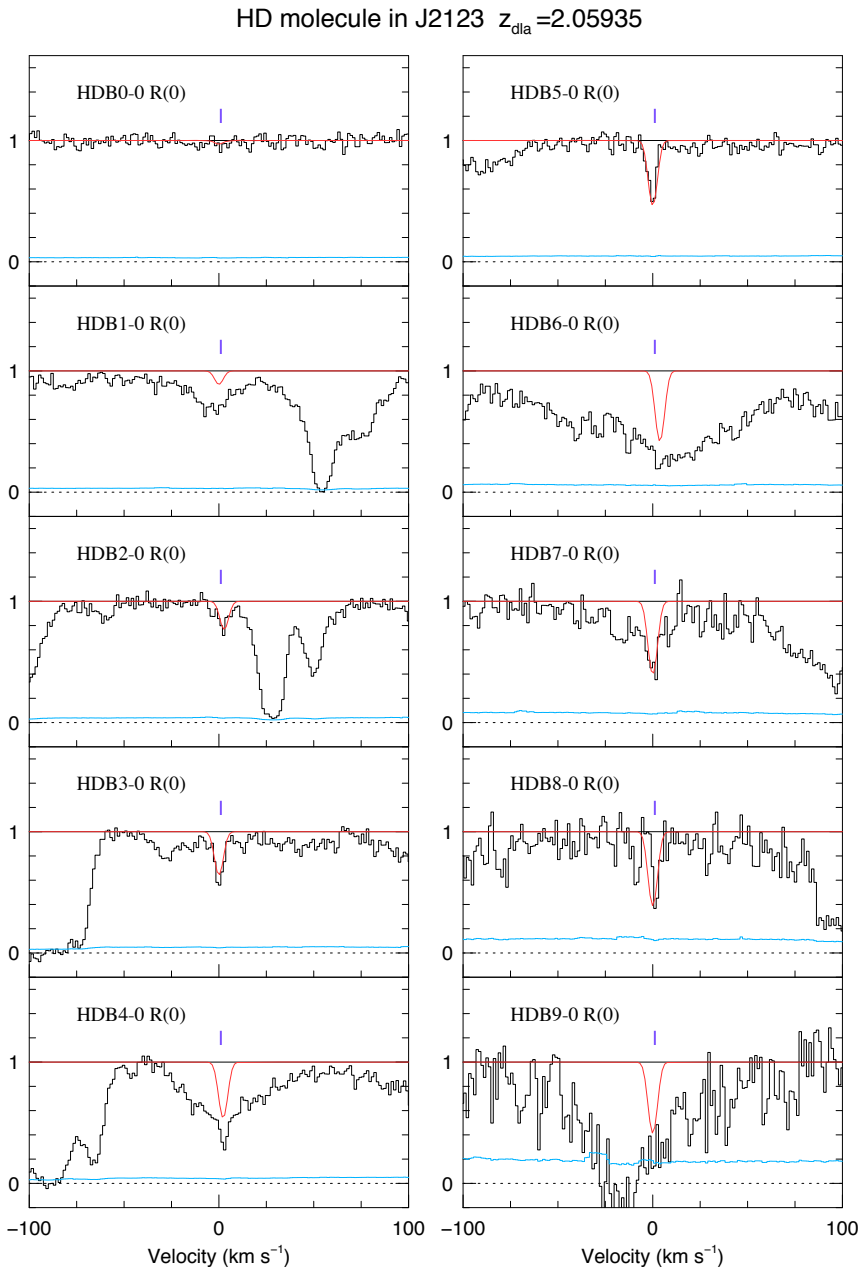

Figure 2.9: Fits to HD molecule Lyman band transition towards J2123−0050 on a velocity scale relative to $z = 2.05930$.

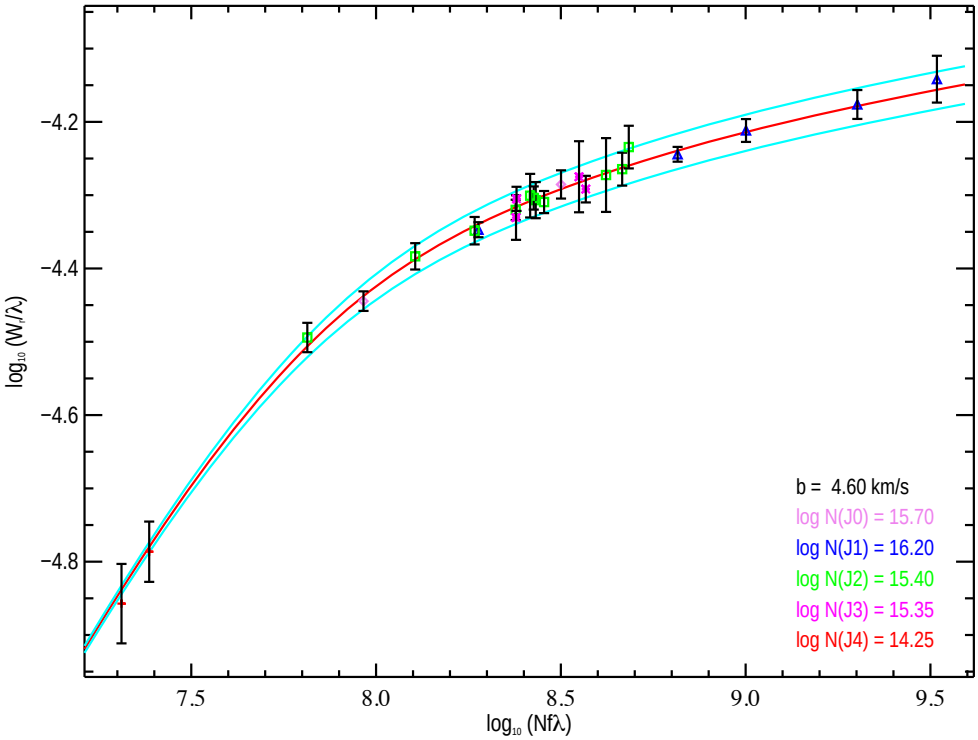

Figure 2.10: Curve of growth for H_2 component at $z = 2.059304$. $J = 0$ level data points are presented with a cross sign, $J = 1$ with triangles, $J = 2$ with green boxes, $J = 3$ with diamonds, and $J = 4$ with a horizontal bar. The solution for the column densities of separate states, as well as the b-parameter is given on the plot. The red curve represents the best fit, while the blue bands give the 3 σ error.

Chapter 3 | *Molecules*

Molecules play an important role in the saga of cosmic star formation by providing the principal means of ISM gas cooling. As gaseous clouds collapse to form new stars, gravitational energy from the collapse is radiated out of the system through molecular emission. Furthermore, along with hydrogen and helium atoms and their ions, molecular hydrogen is among the most abundant species in the Universe (Shull & Beckwith 1982).

3.1 Properties of the Hydrogen Molecule

Here, I provide a brief overview of the notation and physics of molecular lines. I focus the discussion on the H_2 molecule because of its simplicity. A more detailed description of molecular quantum mechanics and H_2 can be found in the reviews by Herzberg (1950), and Field, Somerville, & Dressler (1966).

Molecular hydrogen is a homonuclear molecule, which lacks a dipole moment that forbids transitions in the infrared and radio regions of the electromagnetic spectrum (except the very weak quadrupole transition in the infrared). For this reason, even though it is the most abundant molecule, H_2 is studied less often in astronomy than asymmetric molecules, most notably carbon monoxide. The only way to observe molecular hydrogen in the interstellar medium is through the Lyman and Werner band transitions in UV, which arise through the absorption from the ground electronic level of H_2.

The ground electronic state of the hydrogen molecule is denoted by $X^1\Sigma_g^+$. The

total electronic angular momentum (L) is strongly coupled with the nuclear axis vector. The quantum state of angular momentum is given by $\Lambda=|L\boldsymbol{k}|$, where $\boldsymbol{k}$ is a unit vector along the nuclear axis. States with Λ=0 are denoted by Σ, Λ=1 by Π, Λ=2 by Δ and so on. The various electronic states are labelled alphabetically, with capital letters used for the singlet states, and lower case letters for triplet states. The symmetry properties of the wavefunction are presented with subscripts g and u, and + and −.

Figure 3.1 shows the schematics of the potential energy curves of the ground and a few of the lowest excited states. Each electronic state is split into a set of roto-vibrational levels, corresponding to the motion of the nuclei. The angular momenta of electronic orbital motion L, nuclear rotation R ($R = 0,\ 1,\ 2,\ 3, ...$), and electron spin S ($S = \pm 1/2$) combine to form the total angular momentum vector J, where $J = N + S$, with N being $N = L\boldsymbol{k} + R + S$. In the ground electronic state, electrons have asymmetric spins, so for $S = 0$, the J number is identical to N. The statistical weight of a level is a function of the rotational quantum number and the nuclear spin, specifically $(2J + 1)(2I + 1)$, where I denotes nuclear spin. Since the H_2 molecule has two identical nuclei, only one combination of nuclear spins is possible for each J state, and I is quantized to be 0 (ortho-hydrogen) and 1 (para-hydrogen). For the ground state, all even J states have $I = 1$, hence the statistical weight is $3(2J + 1)$, and all odd ones have $I = 0$, hence the statistical weight is $(2J + 1)$.

Since the selection rules for transitions between the states are $\Delta\Lambda = 0,\ \pm 1$, and $\Delta S = 0$, with symmetry rules applying as well (u to g, g to u, and + to +, − to −), the first allowed transitions to the ground state $X^1\Sigma_g^+$, are from $B^1\Pi_u^+$, and $C^1\Pi_u^+$, and are known as the Lyman and Werner bands. These transitions cover energies from ~ 11 to ~ 14 eV, covering the spectral region from about 844 to 1126 Å.

I use the notation in which the sets of transitions between the two vibrational levels with $\Delta J = -2,\ -1,\ 0,\ 1,\ 2$ are called respectively the O, P, Q, R, and S branches. Hence, I label transitions as <band> ν'-ν'' <branch>(J$''$), where the

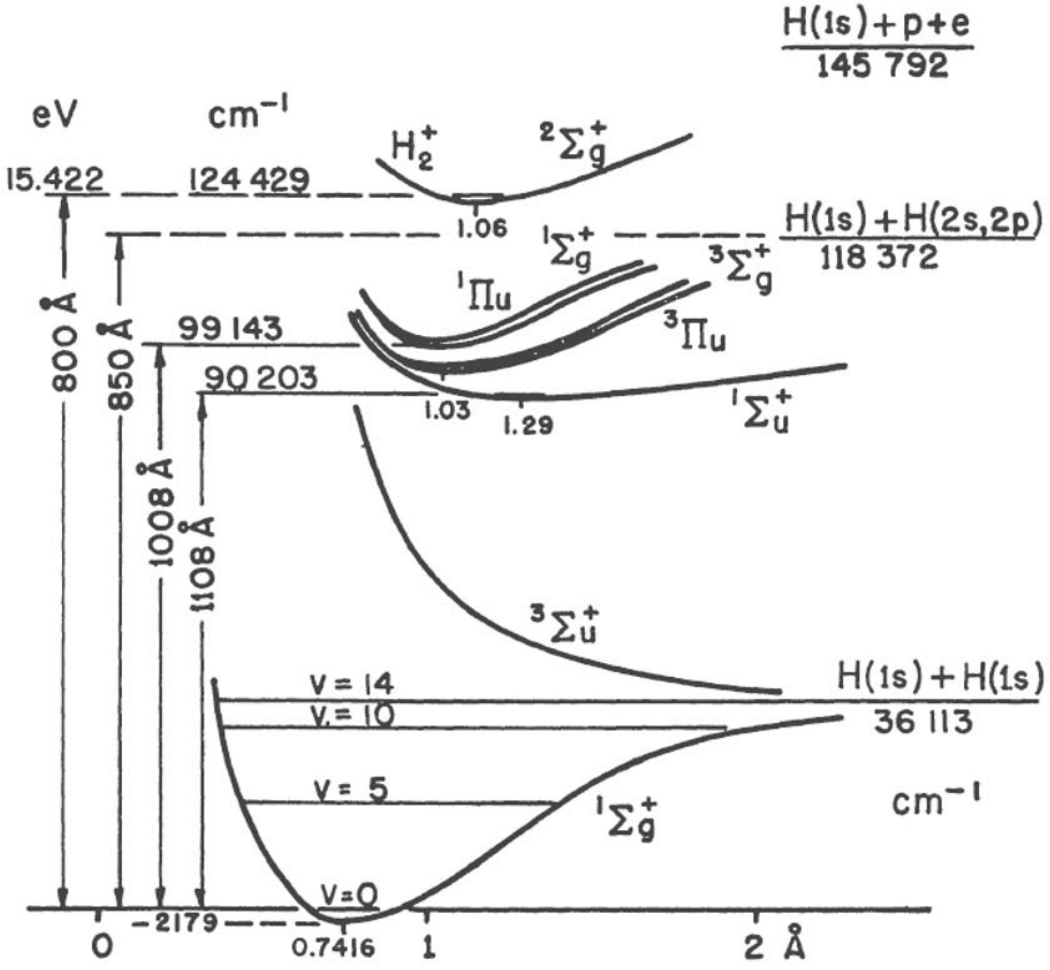

Figure 3.1: H_2 energy level structure from the review by Field, Somerville, & Dressler (1966)

superscripts $'$ and $''$ refer to upper and lower levels. For example, the transition from $B^1\Pi_u^+$ to $X^1\Sigma_g^+$ (Lyman band), from vibrational level 5 to 0, and rotational level 1 to 0 is B5-0R(0).

3.2 Molecules in J2123−0050

The SDLA system at 2.05934 towards J2123−0050 has the lowest measured neutral column density ($\log N(\mathrm{H\,I}\ z = 2.05934) = 19.18 \pm 0.15\ \mathrm{cm}^{-2}$) among the high-

redshift systems with molecular absorption detected to date. Furthermore, this system has a very high metallicity, approaching the solar level (for comparison, an average DLA has [M/H]= −1.2 (Wolfe, Gawiser, & Prochaska 2005)), and hosts multiple carbon fine structure transitions which are thought to be one of the primary coolants of neutral gas in the ISM. Molecular absorption is detected in the Lyman and Werner bands of both the H_2 and HD molecules. The detection of HD in this system is the third published at high redshifts to date (Varshalovich et al. 2001, Noterdaeme et al. 2008).

3.2.1 Molecular Abundances and Kinematics

The results of the molecular line measurements are given in the Chapter 2. Using the described measurement methods, I derived a total column dentisty for H_2 of log$N(H_2)$=16.34±0.03, and log$N$(HD) = 13.89±0.04 cm^{-2} for the deuterated hydrogen molecule. These measurements permit the calculation of the molecular fraction of hydrogen as:

$$f(H_2) = \frac{2N(H_2)}{[N(\text{H I}) + 2N(H_2)]}. \tag{3.1}$$

For the SDLA towards J2123−0050 this value stands at $f(H_2) = 10^{-2.54}$ and it is higher than expected for a system of such a low N(H I) when compared with other measured sightlines in both the local and high-redshift universe.

The HD fraction is calculated as $\log(N(\text{HD})/2N(H_2))$, and in the SDLA towards J2123−0050 the derived value is −2.75. This is an unusually high value when compared with the Galactic sightlines from the FUSE HD survey of Snow et al. (2008), who obtained a range of values from −6.18 to −5.13. This means that either photodissociation of HD is smaller compared to H_2 , or the formation of HD is enhanced. The first scenario is unlikely because N(H_2) is too small to allow even for H_2 to be selfshielded (which happens only at column densities greater than $N(H_2) > 10^{19}$ cm^{-2}). On the other hand, HD forms both on grains as H_2, and via

the gas formation channel through the reaction $H_2 + D^+ \rightarrow HD + H^+$. While in general the HD grain formation rate is lower than the H_2 formation rate because the deuterium atom moves more slowly over the grain due to its size, in special cases (due, for example, to a smaller grain size or higher grain temperature) the efficiency of the grain formation of HD increases (Cazaux et al. 2008). Photon heating of grains is likely to have more impact on the hydrogen molecule, than its deuterated counterparts, because smaller energies are needed to evaporate the hydrogen atom from grains than for the deuterium atom. There have been attempts to relate the measured HD abundance in DLAs with the primordial D/H level. Noterdaeme et al. (2008) measured a high HD fraction in the system towards the quasar SDSS J143912.04+111740.5 that is close to the primordial D/H ratio estimated from the WMAP. They argue that this result indicates a low astration factor of deuterium, which could be explained by an intense infall of primordial gas onto the associated galaxy. However, the HD fraction should be used as a measure of the D/H ratio only in if the gas is predominantly in the molecular form, which is true only in the case of dense molecular cores (Lacour et al. 2005). For this reason, the HD fraction in DLAs and SDLAs is a poor estimate of D/H since the gas is mostly neutral or ionized. For the same reason, the HD fraction in DLAs and SDLAs clearly cannot be used to infer the primordial D/H.

In their VLT/UVES database of molecular hydrogen in high–redshift DLAs, Noterdaeme et al. (2008) find that H_2 is usually detected in very few components (typically one or two), and is kinematically aligned with the strongest metal line components within the system. The authors also suggest that this can be used as an indication that H_2 in DLAs is not associated with the outflows, but it is coming from the bulk of the mass of the system. The molecular absorption in the SDLA towards J2123−0050 is consistent with this finding. The hydrogen molecular absorption is aligned in velocity space with the two strongest metal line components (see Figure 4.2 for a comparison of absorption profiles between metal ions and

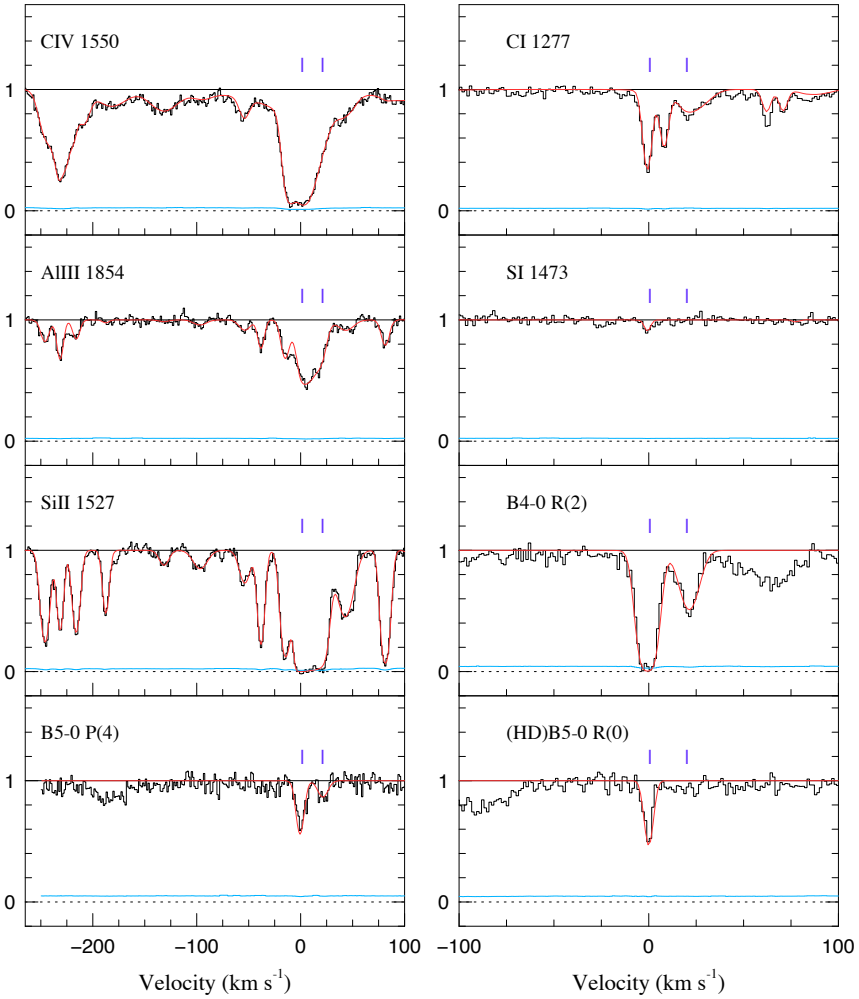

Figure 3.2: Comparison of velocity profiles of absorption features from different ionization phases at the velocity scale relative to z=2.0593. The red line represents the best fit to the absorption profiles. The blue ticks marks indicate the central velocity of the molecular absorption components.

molecules). There is no H_2 absorption detected at the velocities of weaker (satellite) complexes that correspond to the lower column density HI component. The H_2 components are especially well aligned with the neutral metal absorption in CI and SI. This might suggest that the neutral metal absorption occupies the same physical phase as the molecular gas.

3.2.2 H_2 modelling

If the column density of many J level transitions in the H_2 molecule can be obtained, it is possible to derive physical constraints of the molecular gas. For modelling purposes I adopt the code originally developed by Browning, Tumlinson, & Shull (2003) for the FUSE program of observing interstellar H_2 (Tumlinson et al. 2002). This code assumes steady state conditions to calculate the total physical density of the gas in each roto-vibrational level. Such an assumption implies that there is a balance between the population and depopulation of the molecular levels, as well as creation on grains, and more rarely, three-body interactions, and photo and collisional destruction. The primary population mechanisms in the code are spontaneous decays from upper levels, cascades following the absorption of Lyman and Werner band photons, direct formation onto the level, because well as collisional excitation. Similarly, the depopulation mechanisms are radiative absorption out of the level, spontaneous photodecay and collisional deexcitation. Deeper in the cloud, collisional population and de–excitation become more important, as the absorption in Lyman and Werner band lines decreases as the gas becomes self-shielded. This also reduces the photodestruction rate towards the centre of the cloud. The code determines the magnitude of these effects in order to obtain the final result.

The clouds are simulated as isothermal slabs, as is usual in algorithms of this type (for example, CLOUDY assumes a similar geometry). In this geometry, the cloud is illuminated from one side, and it is assumed the additional radiation input is negligible. Since the diffuse clouds that in the model are thought to be in the

vicinity of the radiation field (for example, star forming regions) this is a safe assumption. Browning, Tumlinson, & Shull (2003) discuss this in more detail by performing a calculation in which the modelled cloud is illuminated from two sides with the same incident radiaton field. The authors find that the effects of a change in the geometry are modest, being less than ~ 0.3 dex in the column density of separate J levels using a variety of models with different input parameters. The assumed far-UV incident spectrum is assumed to be flat in the wavelength range of 912 – 1120 Å. The Galactic far-UV spectrum does vary slightly over the wavelengths of interest, but the authors chose not to include this subtle variation in the code since, for the variety of environments that are studied (Magellanic Clouds, or, in this case, a sub-DLA), the Galactic spectrum might be a poor match to the observed spectrum. However, the models performed with a flat spectrum and the often quoted Galactic spectrum of Draine (1978) show very similar results, and the models with the Galactic mean input parameters match very well the Galactic sightlines observed with FUSE (Tumlinson et al. 2002).

The code calculates a multi-dimensional grid of column densities of each J-state by varying the cloud density (n), temperature (T), size (d), UV radiation field strength (I), and grain formation rate of hydrogen molecules (R) which encompasses the whole formation process on the dust grains. The basic algorithm of this process is that formation happens when an H atom collides with a dust grain, and after being adsorbed, moves over the grain surface and encounters a previously adsorbed H atom. The formation rate itself is then primarily a function of metallicity, but also metal abundance, grain type and size, temperature, and sticking factor.

The goal of H_2 modelling is to determine the range of input parameters which matches the observed values. In order to compare the models with the observed values, one can opt for direct comparison of derived J-state column densities to the observed ones. However, even though the modelling technique, and the range of input parameters, covers the primary physical processes which are to be accounted

in molecular line absorption it lacks the sophistication (for example, the further treatment of grains which are a primary catalyst for H_2 formation) which would allow a direct column density comparison. Far more reliable indicators of physical properties of the absorbing system, are the molecular fraction and excitation temperature.

The molecular fraction (Eq. 3.1) of H_2 reduces to the ratio of formation and photodestruction rates, if the cloud is assumed to be homogeneous. In the standard model (Jura 1975, Jura 1975), H_2 is in equilibrium between the formation rate R and photo-destruction rate D, as:

$$Dn(\mathrm{H_2}) = Rn_{\mathrm{H}}n_{\mathrm{H\,I}} \approx f_{diss}\sum_J \beta(J)n(H_2, J) \tag{3.2}$$

where $\beta(J)$ is the photo-destruction rate for the level J, and f_{diss} is the photodissociation coefficient. The photodissociation coefficient varies with the cloud depth and the intensity of the UV spectrum, since collisional effects might dominate deeper in the cloud. For such reasons, f_{diss} is calculated explicitly for each band at each step into the cloud. Its value varies from 0.10 to 0.15. Hence, the molecular fraction is simply a measurement of the balance between the creation and destruction of H_2. The depressed formation rate acts to suppress $f(H_2)$, while the depressed destruction rate enhances it. This effect is presented on the upper panels of Figure 3.3. The clouds that are exposed to a lower incident UV radiation field have a higher molecular fraction for the same total column density as those irradiated with a higher UV flux. Similarly, a lower grain formation rate (R) causes a drop in the molecular fraction.

To further examine the effects of competing destruction/creation processes on the molecular fraction, consideration of the rotational excitation of H_2 provides a useful diagnostic. When a photon is absorbed the molecule excites into the upper electronic state. What follows is emission as molecules cascade down through the rotational and vibrational states to the ground electronic state. As a net effect of

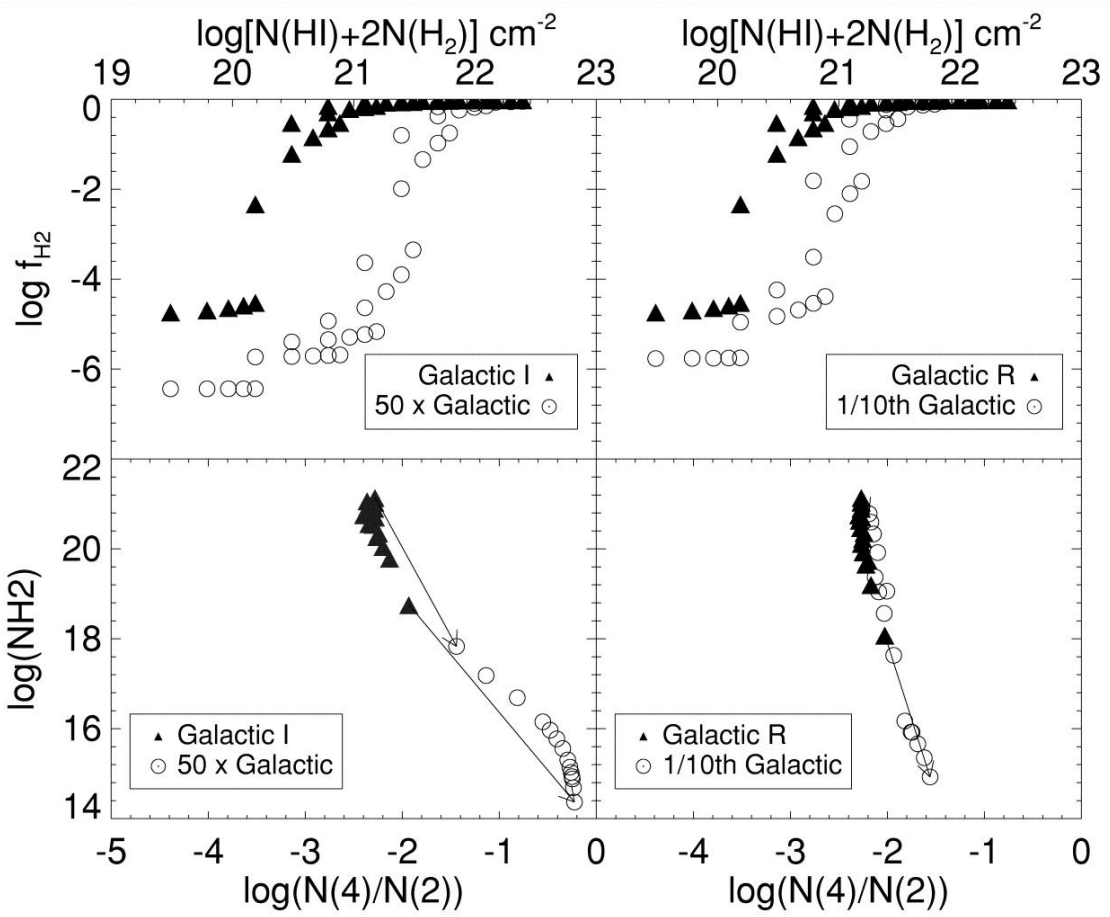

Figure 3.3: H_2 modelling Diagnostic (Browning, Tumlinson, & Shull 2003). When exposed to a lower incident UV radiation field the systems have a higher molecular fraction for the same total column density as those radiated with a higher UV flux (left panels). Similarly, a lower grain formation rate (R) causes a drop in the molecular fraction (right panels).

all of the absorptions within the cloud, and the cascades that follow, the molecules are redistributed into rotational levels of the ground state. This distribution can be observed by determining the column density of each of the rotational levels $N(J)$ from the line measurements, as is given for J2123−0050 in Chapter 2. The ratios

of these column densities give the excitation temperature:

$$T_{J''J'} = \frac{\Delta E_{J'J''}/k}{ln[(g(J'')/g(J')) \times N(J'')/N(J')]} \tag{3.3}$$

where superscripts $'$ and $''$ refer to upper and lower levels, and $g(J'')$ and $g(J')$ are statistical weights. The g ratio for J levels 0 and 1 is g_1/g_2=9, and $\Delta E_{01}/k$=171 K, so that T_{01}, the rotational temperature, is simply $T_{01} = 171\ K/\ln(9N(0)/N(1))$. At densities and cloud depths high enough (corresponding to extinctions of $A_\nu > 2$) for collisions to dominate the populations of levels J=$\{0,1\}$ (as in translucent clouds), the rotational temperature traces the kinetic temperature. In diffuse clouds (as DLAs and SDLAs are most likely to be), the relation between these two quantities is not precisely known (Tumlinson et al. 2002), but for diffuse clouds of H_2 with total column density near the upper end of the distribution ($N(H_2)$>10^{16} cm^{-2}), T_{01} still provides a good tracer of T_{kin}. It is possible to determine similar temperatures using higher J levels, but these are less sensitive to the kinetic temperature (collisional processes), and much more sensitive to the radiative cascade (radiation field). The ratios of $N(4)/N(2)$, and $N(5)/N(3)$ are especially likely to probe the strength of the radiation field. The lower left-hand panel of Figure 3.3 ilustrates the effect of increasing the radiation field as $N(4)/N(2)$ increases. The lower right-hand panel, however, shows that changing the grain formation rate makes almost no change to the same J level ratios.

3.2.3 Physical Properties of Molecular Cloud Phase

I ran the grids with the input parameters in the range of: $I = \{1{:}100\} \times 10^{-8}$ cm^{-2} s^{-1} Hz^{-1}, $R = \{0.03{:}3\}$ $\times 10^{-17}$ cm^3 s^{-1}, n$_H$ = $\{1{:}800\}$ cm^{-3}, $d = \{1{:}10\}$ pc, and $T_{\rm kin} = \{10{:}150\}$ K, which produces 4707 grid points in total. The results are presented in Figures 3.4 and 3.5 along with the measurements from previously published H_2-bearing QAL systems, as well as Galactic and Magellanic Cloud sightlines. The red open squares present the models produced with input parameters

which are representative of Galactic conditions ($I = \{1 : 4\}$ 10^{-8} cm^{-2} s^{-1} Hz^{-1}, $R = \{0.3 : 3\}$ 10^{-17} cm^{3} s^{-1}), while the green ones reproduce conditions in the Magellanic Clouds ($I = \{10 : 100\}$ 10^{-8} cm^{-2} s^{-1} Hz^{-1}, $R = \{0.3 : 3\}$ 10^{-17} cm^{3} s^{-1}). Both grids are then calculated by varying other input parameters (temperature, density and cloud size). Raw column density measurements place SDLA in J2123−0050 in a position which does not match the modeled local universe conditions.

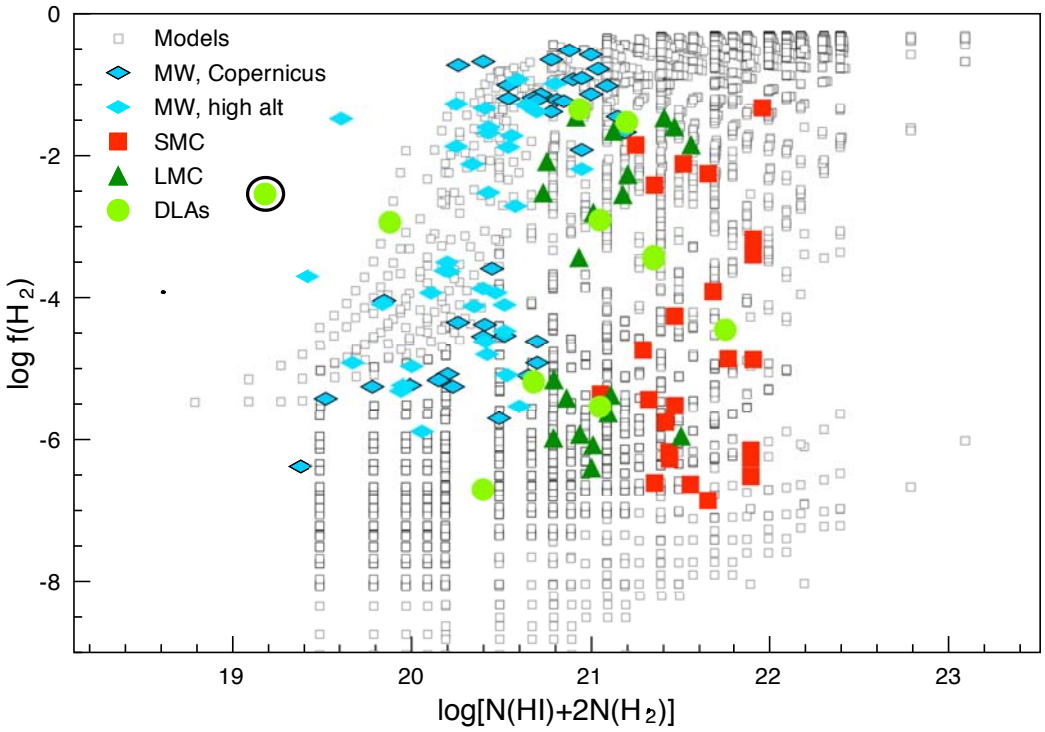

Figure 3.4: The QAL systems (green filled circles), Galactic (light blue diamonds), and Magellanic Cloud (red squares for SMC, and green triangles for LMC) sightlines molecular fraction compared to the model grids (opened blue for Galactic conditions, and red for Magellanic Cloud conditions). The position of the SDLA towards J2123−0050 (marked with black open circle) is unusual since such a high H_2 fraction is not expected for such a low N(H I).

To further determine the position of the system within the physical parameter

space, I examined the excitation temperatures of the system in comparison to the model grids. The data are presented in Figure 3.5. The rotational temperature of the system $T_0 = 163$ K, is found to be higher than the average rotational temperatures measured in Galactic and Magellanic Cloud sightlines (as seen in the upper left-hand panel of Figure 3.5). Since this temperature differs greatly from both the average translucent and diffuse cloud kinetic temperature, photoexcitation must play an important role in the redistribution of H_2 in its rotational levels. Along with the high value of $N(4)/N(1)$, this indicates an enhanced radiation field, and a lower grain formation rate, as discussed in the modelling diagnostic paragraph of this text. Hence, the SDLA in J2123−0050 is created by absorption within a cloud that is radiated with a UV flux of the order of a couple of Galactic intensities, and a grain formation rate that is approximately half of the Galactic average. The grain formation rate is depressed in this environment by the high incident UV photon flux.

In summary, this chapter presents evidence that the SDLA towards J2123−0050 is in a region that has not only been previously enhanced by metals, but also with molecules. The modelling indicates that nearby star formation may still be ongoing. However, the H_2 fraction is puzzling. I return to this issue in Chapter 5.

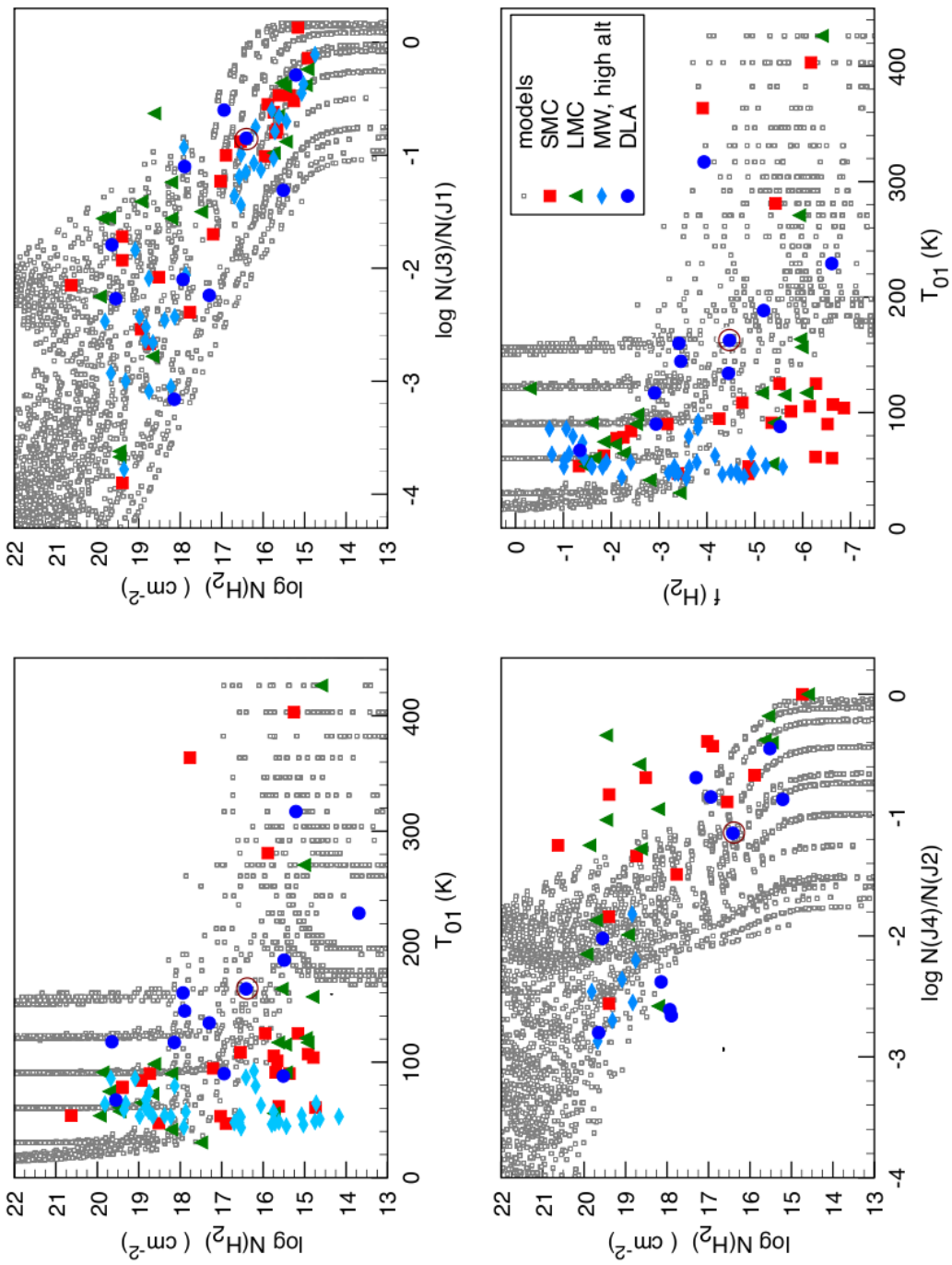

Figure 3.5: Various results concetning the excitation temperature of H_2. The data points are labeled as in Figure 3.4. The upper right panel presents the rotational temperature. The upper left-hand and lower-hand right panel present a column density ratio of higher J states compared to the total H_2 column density. The lower left panel gives the rotational temperature vs. the H_2 fraction. In all of the panels the SDLA towards J2123−0050 occupies the position among the locus of models

Chapter 4 | *Metals*

While most of the mass density of light elements such as hydrogen, helium and lithium hails from nucleosynthetic origins in the big bang, metals are predominantly produced in stars. The interplay between the metal production in stars and the feedback processes that return elements back to the interstellar medium has an important role in the creation and evolution of galaxies over cosmic time.

Metals in the local ISM have been studied extensively for more than a century. In 1904 Hartmann discovered stationary lines of Ca II in the spectroscopic binary δ Orionis (Hartman 1904). The single narrow profile led the author to suggest that these lines are formed in a single cold (T<1,000 K) cloud. Shortly after, it was demonstrated that the space between these cold interstellar clouds is filled with a widespread warm interstellar gas (Trumpler 1930). Today we describe the ISM as a medium that exhibits a complex multiphase structure (Field, Goldsmith, & Habing 1969, McKee & Ostriker 1977, McKee 1995). The coldest ISM phase (Cold Neutral Medium – CNM) is concentrated in a small fraction of the volume, but contains much of the total neutral hydrogen mass. The warm phase (Warm Neutral Medium – WNM), on the other hand, is widespread, filling much of the volume occupied with the neutral ISM, but contributes a smaller fraction to the total mass budget (McKee 1995). The presence of diffuse ionized gas in the Galaxy was also revealed in the radio part of the electromagnetic spectra according to the study of Hoyle & Ellis (1963). The Warm Ionized Medium (WIM), as this phase is called, is the principal component in the total mass budget of the interstellar medium in our Galaxy and others. The photoionizing radiation from OB star associations

penetrates the interstellar medium and ionizes much of the neutral hydrogen. The ionization from these stars creates regions of H II dominated gas within which hydrogen is almost fully ionized (Stromgren spheres). However, the presence of the WIM extends far beyond the Stromgren spheres. Hα surveys (Sivan 1974, Reynolds et al. 1986, Reynolds, Haffner, & Tufte 1999) detected diffuse Hα emitting gas in all directions around us. The Hα maps show a complex structure of filaments, patches and loops. It is likely that this filamentary structure allows photoionizing radiation to leak through the well defined HII regions deeper into interstellar space, ionizing the gas in lower density portions of the ISM. The neutral ISM phases are, as a result, immersed in the diffuse ionized gas that occupies much of the Galactic volume, extending a kpc above and below the plane of the Milky Way (Reynolds et al. 1986).

The Hot Ionized Medium (HIM) fills the bubbles of the ISM carved out by the ionizing radiation from young OB stars (McKee & Ostriker 1977), but also exists in the form of hot galactic coronal gas which provides necessary pressure to confine the observed high-altitude Galactic ISM clouds (Spitzer 1956). Furthermore, this gas has been detected in the broad UV high-stage metal ion absorption lines (O VI $\lambda\lambda 1032, 1038$, N V $\lambda\lambda 1239, 1243$) from hot young stars with the *Copernicus* satellite (Jenkins & Meloy 1974, York 1974). The ecology and evolution cycle of the ISM is presented in Figure 4.1.

At high redshifts ($z \geq 2$), direct observations of the ISM are limited to a handful of objects characterized by unusually high star formation rates (on the order of tens, or even hundreds of solar masses per year), such as super-luminous sub-mm galaxies (Holland et al. 1999), or LBGs (Pettini et al. 2002). However, the relatively low apparent magnitudes of these high-z objects limits our observations and makes it difficult for us to precisely probe the abundances and kinematics of the multiphase high-z ISM. In the case of the lensed LBG cB58, Pettini et al. (2002) succeeded in obtaining relatively high resolution data. They found that the ISM of cB58 is

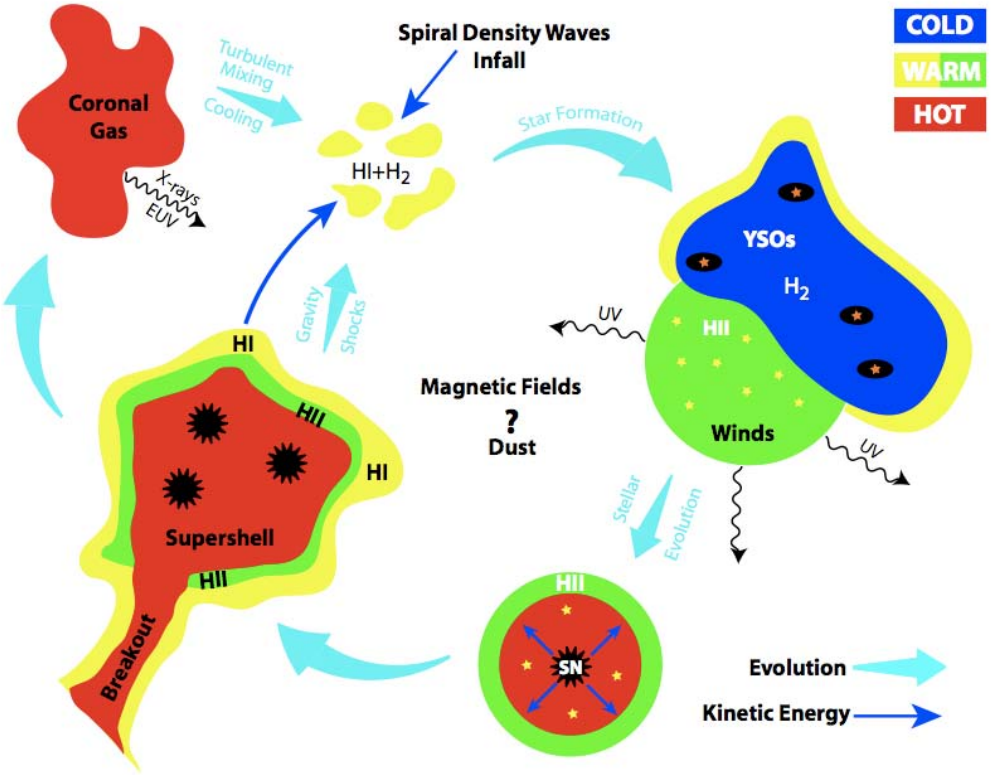

Figure 4.1: Cartoon representation of ISM ecology by Tumlinson (2006). The colours differentiate separate ISM phases – blue represents the cold medium (molecular clouds), yellow and green the warm medium (CNM, WNM, and WIM), and red the hot medium (HIM). The arrows show the direction of evolution giving the simplified version of the evolution cycle of the Galactic ISM.

heavily enriched by supernovae type II ejecta (α-enhanced), and that even at such an early epoch (z≈2.7) this galaxy has efficiently processed its gas reaching a high metallicity of about 2/5 solar. However, objects like LBGs or sum-mm galaxies host some of the most extreme star-forming regions in the universe and might not necessarily be representative of the global properties of the non-local ISM. Indirect observations, through the intervening absorption in quasar and GRB spectra are a powerful alternative for probing the ISM gas in the high redshift universe.

DLAs and SDLAs, as the main contributors to the neutral gas mass budget at all redshifts, provide a window into galaxy evolution that allows us to trace the consumption of gas as it is turned into stars over cosmic time. It has been suggested that DLAs contain sufficient mass in neutral-gas at high redshifts to account for a high fraction of the visible stellar mass density of the present day universe (Wolfe, Gawiser, & Prochaska 2005). Furthermore, both DLAs and SDLAs offer a direct and accurate probe of elemental abundances throughout much of the history of the universe. In particular, the abundance studies of these high N(HI) column density QAL systems aim to cast light on the early stages of galactic evolution and probe the nucleosynthetic processes at work in proto-galactic environments (Lu, Sargent and Barlow 1996, Pettini 1997, Prochaska & Wolfe 1999, Molaro 2000, Charlton 2003, Herbert-Fort et al. 2006, Péroux et al. 2007).

Because of the high neutral hydrogen column densities of DLAs, gas self-shielding, and the ionization potential of the metal species, it is often assumed that the column density of singly ionized transitions approximates the total column density of the metal (N(X)=N(XII)). As a consequence, ionic abundances can be considered to be close to the total abundances for a given element. However, at lower neutral hydrogen column densities (as in SDLAs) this approximation may no longer hold and a significant fraction of the column density of metal species occur in higher ionization states. The ionization effects on the abundance is the most severe in the case of SDLAs. However, even though the high total column densities of DLAs

would suggest that they are mostly neutral in the case of a monolithic cloud, these systems might be made up of multiple lower column density absorbing clouds residing at similar velocities along the line-of-sight. In this case, ionization corrections would be necessary in the abundance studies of DLAs. For example, Prochaska et al. (2002) found a DLA toward GB 1759+7539 with a significantly ionized phase present.

Studies of the ionization properties of QALs have been made easier by the development of the photoionization code CLOUDY (Ferland et al. 2001). The main difficulty of photoionization modelling of QALs is choosing the right strength and shape of the ionizing radiation field (even though some questions have been raised regarding uncertain physics involved in CLOUDY photoionization modelling — see Prochaska et al. 2002). In recent studies (Howk & Sembach 1999, Vladilo et al. 2001, Izotov, Scharer & Charbonnel 2001, Prochaska et al. 2002, Dessauges-Zavadsky et al. 2003, Peŕoux et al. 2007) the authors usually opt for an external spectrum comprised of integrated light from QSOs, AGNs and galaxies (Haardt & Madau 2001), and some version of an internal spectrum from stellar sources (usually some integrated spectrum of typical late-O star associations — see, e.g., Kurucz 1991, or D'Odorico & Petitjean 2001). While there is general agreement that the level of corrections is negligible for the high-end column density absorbers (DLAs), current results for the lower-end column density systems (SDLAs) are often contradictory. For example, Vladilo et al. (2001), and Dessauges-Zavadsky et al. (2003) find that the ionization correction for SDLAs are within 0.2 dex. On the other hand, Howk & Sembach (1999), and Prochaska et al. (2002) argue that ionization effects causing abundance corrections even as little as 0.2 dex may still significantly influence our interpretation of intrinsic abundance ratios (especially for Si/Fe and Zn/Cr) implying different dust-depletion patterns, and different nucleosynthetic histories.

To probe the influence of these effects on our understanding of the high-redshift

ISM, I present a detailed study of an extraordinary high-redshift SDLA towards J2123−0050. In this chapter, I will provide clues about the multiphase nature of the absorber's ISM through a study of its kinematic structure, and ionization properties. Furthermore, I will examine the implications of the multiphase nature of the ISM on deriving the ionization corrections which are a necessary step in deriving the elemental abundances of SDLA.

4.1 The Multi–phase ISM in the SDLA towards J2123−0050

The SDLA at z=2.05934 towards J2123−0050 is a kinematically complex system with metal absorption lines spreading over $\sim$ 400 km s^{-1} in velocity space. Figure 4.2 compares the metal absorption in the different ionization stages to neutral hydrogen, and molecular absorption. The molecular lines align with the strongest metal velocity components.

The velocity profiles of selected metal ion transitions are presented in Figures 2.6, and 2.7, in Chapter 2. The Voigt profiles presented along with the data were fitted in order to obtain the total column density of ions. The choice of the number of velocity components does not necessarily reflect the real kinematic structure of the system (for more discussion consult Section §2.3). Nevertheless, the fifteen component fit does allow a general insight into the complex kinematic structure of this absorber. Visual inspection of the system's kinematics unravels the two distinct metal absorption complexes centred around redshifts of 2.05684 (satellite complex) and 2.05934 (main complex).

The satellite complex is weaker in absorption strength (for b-parameter and column density measurements check Tables 2.2–2.5 in Chapter 2) with ionized metal species transitions detected (from Si, C, Al and Fe). However, this complex does not give rise to absorption in neutral metal species, nor in molecular gas, which is

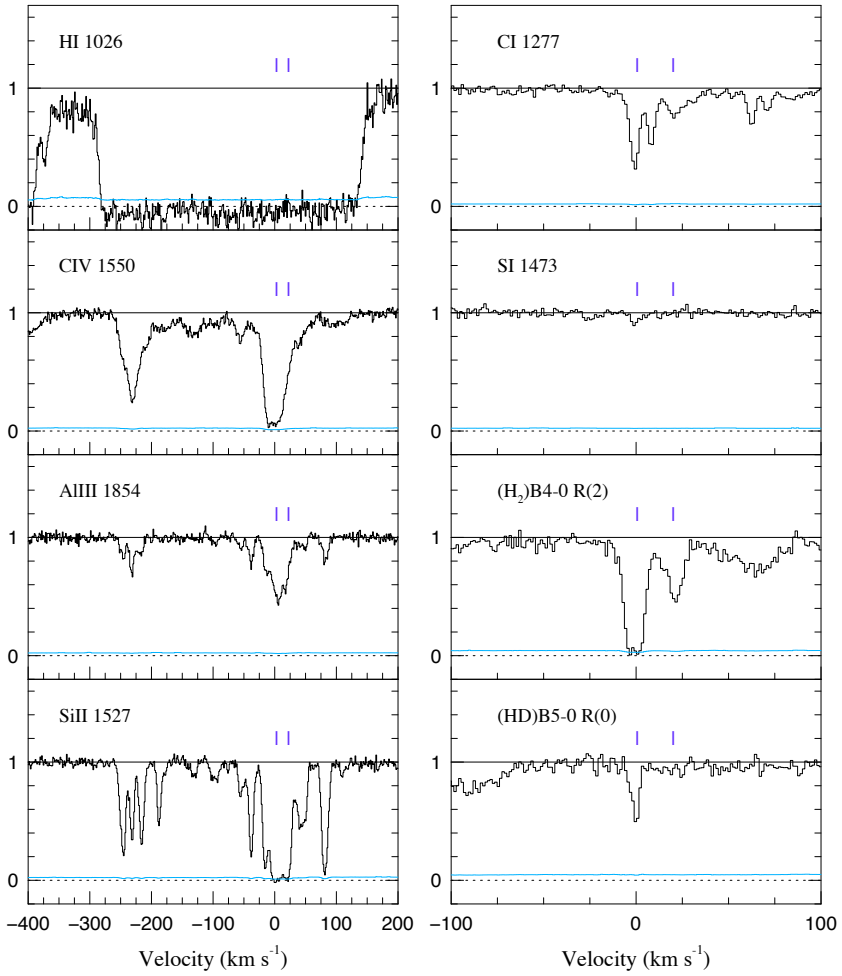

Figure 4.2: Comparison of the absorption in neutral, ionized and molecular gas in velocity space. The blue tick marks indicate the central velocity position of the H_2 absorption components.

likely due to the low HI column density of 18.40 ± 0.3 cm^{-2} measured from the blue wing of the Lyα line. On the other hand, the stronger, main absorption complex, has a neutral hydrogen column density of 19.18 ± 0.15 cm^{-2} which traditionally places this sub-system within the sub damped Lyα absorbers class.

The main complex occupies the velocities from about -110 up to about $+125$ km s^{-1} with respect to the strongest absorption component at $z = 2.05934$. The absorption is detected in metal ions, but also in neutral metal species. The strongest absorption components of the most prominent metal transitions (for example OI λ1039 Å, CII λ1335 Å, SiIII λ1207 Å etc.) occupy the velocity space between ~ -25 and $\sim$50 km s^{-1} and appear saturated. These velocity components also give rise to a variety of neutral metal line transitions of carbon and sulphur, including fine structure transition lines of carbon, as well as molecular absorption.

Since the main complex contains the bulk of the neutral hydrogen, and it exhibits absorption from neutral, molecular and ionized species, it is the best candidate for an analysis of the high-redshift ISM (all the results in this chapter will therefore refer to the velocity space occupied by the main complex absorption). Furthermore, the following properties of the metal absorption in the main complex point to the multiphase nature of the ISM of SDLA towards J2123−0050:

- The absorption from the neutral lines of carbon, as well as the molecular hydrogen is detected in only one out of 10 velocity components which are detected in singly ionized, and highly ionized species.

- The neutral lines of carbon and sulphur match the velocities of the ionic lines according to the best Voigt profile fits. However, they require a small b-parameter of only 1.83 ± 0.30 km s^{-1}, whereas weaker singly ionized species transitions (like SII λ1254 and SiII λ1808) can be unambiguously fitted with only a single, broader ($b = 4.84 \pm 0.12$ km s^{-1}) Voigt profile.

- The presence of significant amounts of highly ionized species such as AlIII,

and Si III requires a separate, warmer gas phase from the one which gives rise to the neutral gas species, such as neutral carbon, or sulphur.

4.2 Elemental Abundances

Abundance measurements of QAL systems are often affected by dust and ionization (Vladilo et al. 2001, Prochaska et al. 2002, Dessauges-Zavadsky et al. 2002). Some of the elemental mass might be depleted and locked in dust grains, and therefore appear absent from the measured gas phase causing an underestimate of the elemental abundance. On the other hand, ionization redistributes the mass between the ionization states of metal species, and hydrogen, which may introduce an overestimate of elemental abundances.

The raw total abundances of measured metal species for the main absorption complex are given in Table 4.1, relative to the Grevesse, Asplund, & Sauval (2007) solar abundance scale that is given in the same table. The raw measurements yield a supersolar metallicity ($[S/H]_{raw} = +0.36$). However, to recover the real metallicity that is not biased by ionization effects one needs to derive ionization corrections. In this section I study the biases of the standard method of deriving these corrections, discuss the findings, after which I derive the corrections for J2123−0050 and apply them to the raw abundances.

4.2.1 Ionization corrections

To investigate the effects of photo-ionization on the abundance measurements authors often perform photoionization modelling assuming that most of the gas resides in a single phase (see for example Howk & Sembach 1999, Vladilo et al. 2001, Prochaska et al. 2002, Dessauges-Zavadsky et al. 2003). This simple scenario is justified by the fact that the narrow absorption lines of C I and S I, which indicate the presence of the coldest, separate, gas phase, are often absent in the spectra of

SDLAs, whereas highly ionized species (such as CIV and SiIV), if detected, contribute only a negligible fraction of the total column density in a certain metal species. However, the J2123−0050 spectrum contains multiple strong neutral lines of carbon and sulphur. Furthermore, some of CI lines are even saturated in this high-resolution spectrum. The strength and narrow profiles of these lines, as well as the presence of strong AlIII absorption suggest that the ISM of this high-redshift object has a multi–phase nature. Calculating corrections on the basis of a single–phase model would introduce a systematic error in the final result. However, an accurate model of the multiphase structure is hampered by our inability to measure what fraction of the neutral hydrogen is in each phase (a necessary input to CLOUDY's model parameters). It is nonetheless possible to estimate the induced error in the ionization corrections if one assumes a single phase model for a theoretical cloud which is actually composed of a two phase medium. In the next section, I make the first quantitative estimate of this effect.

The Effects of Single-phase Modeling on Recovered Metallicities

The following experiment was designed to simulate the process of deriving the ionization corrections based on the real observations. The scenario is as follows:

- The modelling of two-phase gas clouds was performed in CLOUDY. The "cold" phase gas was set to reside in an environment with an ionization parameter of $\log U = -4.96$, while the "warm" phase was set to $\log U = -2.96$. The total combined neutral column density of the cloud in both phases was set to be $N(\mathrm{H\,I}) = 10^{19.18}$ cm^{-2}. To simulate the UV radiation environment of the absorber I opt for a mix of the Haardt-Madau (H&M) extragalactic spectrum (Haardt & Madau 1996), as an external radiation component, and the average Galactic ISM spectrum of Black (1987) as an internal radiation component. The choice of the UV background is dictated by the fact that Galactic ISM diffuse clouds of a similar column density are submerged in sim-

ilar radiation field (Tumlinson et al. 2002). The metallicity was chosen to be [M/H]=−0.33, and the chemical composition of the cloud was set to match the solar abundance pattern as given in CLOUDY version 07.02, which was used to generate these models. Each of the modeled clouds was assumed to have a different ratio of HI column densities in the warm and cold phase ranging from completely cold to completely warm gas (essentially these extrema are single-phase clouds). The phases are modeled by separate CLOUDY runs. The column densities of FeII, SiII, SII, AlII and AlIII ions of a specific cloud are calculated by adding the contribution from the both phases. The final total column densities constructed in this way simulate the information that observer would measure if these clouds were in fact real objects.

- The next step was to simulate the effects of applying the single-phase model derived ionization corrections by trying to recover the metallicity of the theoretical cloud. Two kinds of grids of CLOUDY models are derived for each of the theoretical clouds. One has a metallicity of [M/H]= −0.33, identical to that used to model the theoretical cloud, and the other uses the abundance of singly ionized iron of the theoretical cloud as a metallicity constraint, [M/H]=[FeII/HI]. All grids are calculated using a mix of the Haardt-Madau (H&M) and the average Galactic ISM spectrum stopping the calculations when the column density of neutral hydrogen reaches $N(\mathrm{HI}) = 10^{19.18}$ cm^{-2}.

- The ionization state of the single-phase model of each of the theoretical clouds was inferred from the column density ratio of the adjacent aluminium ions, e.g., AlII/AlIII. Column density ratios of metal ions (like (AlII/AlIII), (FeII/FeIII) and (SiII/SiIII)) are commonly used to determine the ionization parameter in SDLAs and DLAs (Dessauges-Zavadsky et al. 2003, Prochaska et al. 2002). Furthermore it has been shown that the (AlIII/AlII) ratio anti-correlates with the neutral hydrogen column density (Vladilo et al. 2001,

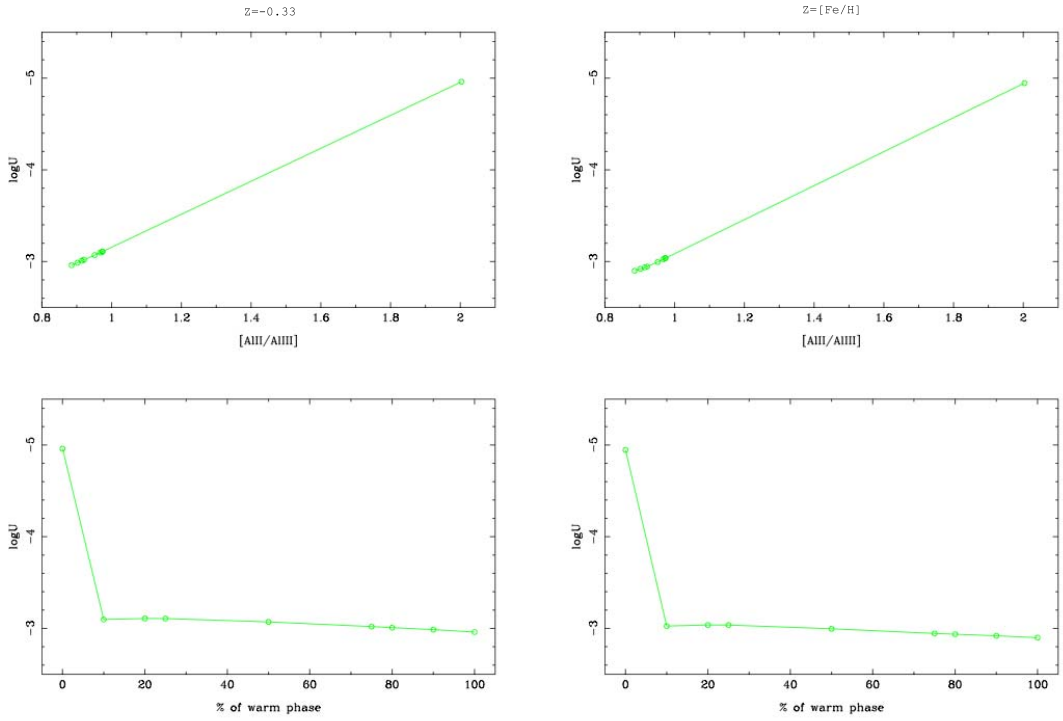

Figure 4.3: The figure presents the derivation of the ionization parameter from aluminium ionic ratios calculated for theoretical clouds. The top panels show a tight correlation between AlII/AlIII and log U, as is expected for this theoretical consideration. The lower panels show the ionization parameter vs percent in which the "warm" phase contributes to the total neutral hydrogen column density. The left hand column is for the single-phase models that assume [M/H]= -0.33, while the right is for models with [M/H]=[FeII/HI]. Remarkably, even if the contribution of the warm phase is as small as 10% the models recover the log U of the warm phase to within $\sim$0.10 dex.

Dessauges-Zavadsky et al. 2002). Narayannan et al. (2008) recently demonstrated that this anti-correlation extends also to the lower N(HI) QALs. The ionization parameter log$U$, defined as:

$$\log U = \log \frac{n_\gamma(\mathrm{cm}^{-2})}{n_H(\mathrm{cm}^{-2})}, \tag{4.1}$$

is determined by matching the aluminium ionic ratio observed in the theoretical clouds to the values inferred from the single-phase grid of models. Figure 4.3 presents the results for each of the theoretical clouds. As expected from this theoretical consideration AlIII/AlII shows a very tight linear correlation with log U. Remarkably, this method was highly efficient in recovering the ionization parameter of the "warm" phase even if its contribution to the total neutral hydrogen density was as small as 10%. The difference between the real and recovered log U for the "warm" phase was only on the order of 0.10 dex.

- After the ionization parameter was derived for each cloud, the ionization corrections are calculated. For each of the ionization parameters (eg. clouds) the code outputs the ionization fractions $f(\mathrm{X}^{i+}) = \frac{n(\mathrm{X}^{i+})}{n(\mathrm{X})} = \frac{N(\mathrm{X}^{i+})}{N(\mathrm{X})}$ in a given metal ion, and the fraction of hydrogen number density in the neutral state $f(\mathrm{HI}) = \frac{n(\mathrm{HI})}{n(\mathrm{H})} = \frac{N(\mathrm{HI})}{N(\mathrm{H})}$. The ionization correction IC(X/H) are calculated from the next equation:

$$IC(\mathrm{X/H}) = \log\left(\frac{N(\mathrm{X}^{i+})}{N(\mathrm{HI})}\right) - \log\left(\frac{N(\mathrm{X})}{N(\mathrm{H})}\right) \tag{4.2}$$

which was simply:

$$IC(\mathrm{X/H}) = \log\left(\frac{f(\mathrm{X}^{i+})}{f(\mathrm{HI})}\right), \tag{4.3}$$

These values are subtracted from the ionic abundances to get the final abundance of a metal.

The results of this experiment are presented in Figure 4.4, for the case in which the metallicity used in the single-cloud model matches the one used in producing

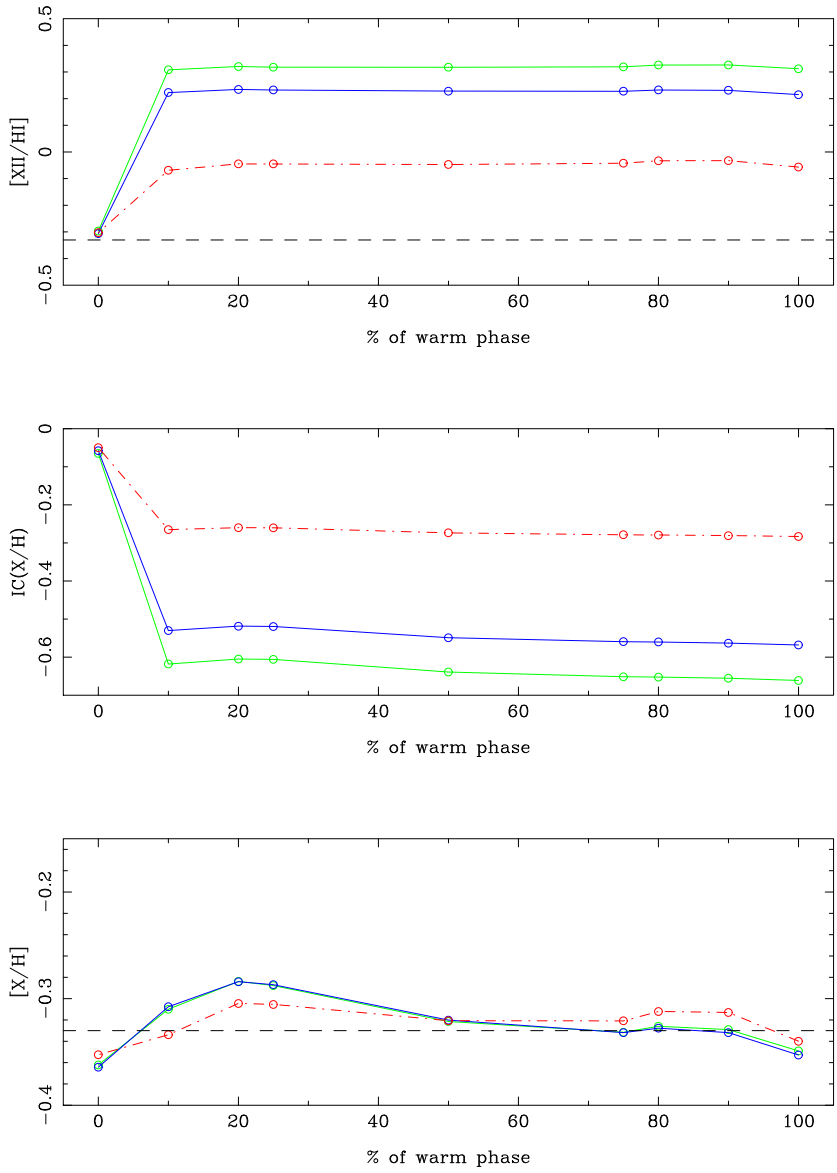

Figure 4.4: Ionization Corrections For Theoretically Modeled Cloud with [M/H]=-0.33. The measured ionic abundances (raw metallicities) are presented on the top panel for SiII (green line), SII (blue line), and FeII (red dotted line). The ionization corrections are given in the middle panel, while the corrected abundances are shown in the bottom one. The black line presents the metallicity of [M/H]= -0.33 for which the theoretical multi-phase clouds are constructed. The single-phase based corrections recover the metallicity of the clouds within an error of $\sim$0.15 dex.

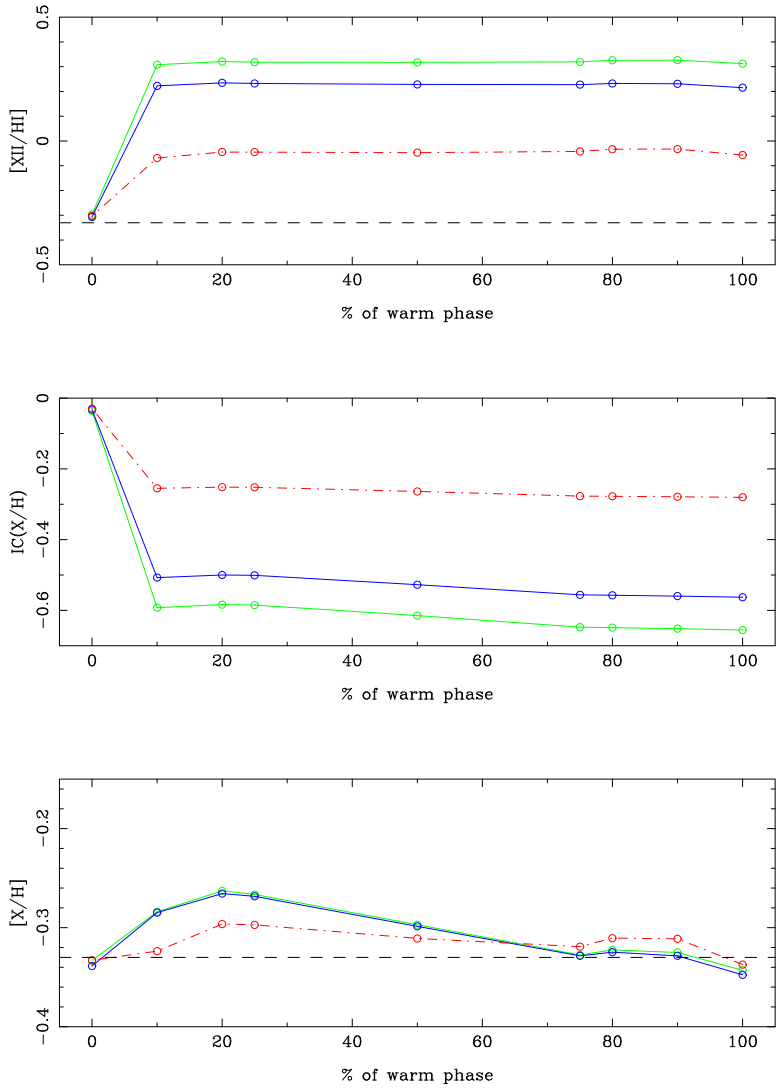

Figure 4.5: Same as in Figure 4.4, but for a metallicity of [M/H]=[FeII/HI].

theoretical clouds, and Figure 4.5, for the case of "observed" metallicity. The top panel presents the "observed" ionic abundance for SiII (green), SII (blue) and FeII, the middle one gives the ionization corrections, while the bottom panel gives the corrected metallicities. The black line presents the metallicity of [M/H]= −0.33 for which the theoretical multi-phase clouds are constructed. The recovered metallicity for all the models in which both phases contribute to the total column density differs from the real metallicity of the cloud. However, the deviation from the [M/H]= −0.33 value is less than 0.15 dex for both kinds of the models. This result gives legitimacy to using a single-cloud approach deriving the ionization corrections for SDLA in J2123−0050, while keeping in mind that the precision of the final metal abundances is ~ 0.15 dex.

The Photoionization Properties of J2123−0050

Following the prescribed single-phase model algorithm a grid of CLOUDY models was derived to investigate ionization corrections for the SDLA towards J2123−0050. In order to simulate the physical environment of the absorber, I adopt a neutral column density of $10^{19.18}$ cm^{-2} (the column density of the main complex), metallicity of +0.32 (from the raw measurement of [SII/HI]), and the solar abundance pattern. The abundance of sulphur is used as a metallicity indicator because iron is likely to be heavily depleted (see the next section). As discussed later, the exact result of the modelling is relatively insensitive to the precise metallicity adopted. We then apply the same model strategy as described in the previous section for a single phase model, but now using the true observed column densities.

In order to determine U the code matches the observed (SiII/AlIII) ratio of 1.25 to the values obtained from the model (see top panel of Figure 4.6). SiII is used as a proxy for AlII since the only available AlII line is saturated and only a lower limit to aluminium ionic ratio (AlII/AlIII$>$ 2.8) can be measured from the available spectrum. Of all the measured species silicon has the most similar

ionization potential to aluminium which provides the rationale for adopting it as a proxy in this case.

The upper panel of Figure 4.6 presents the aluminium ionic ratio (SiII/AlIII) versus the ionization parameter from the model grid. The observed ratio of ions intercepts the model curve at the ionization parameter of $\log U \sim -2.11$, with the error of the single-cloud modelling technique on the order of 0.1 dex. The lower panels give the inferred ionization fraction and correction curves for the ions of interest.

In order to examine the influence of the photoionizing spectrum and the assumed metallicity on the magnitude of the inferred corrections I produced additional grids of models by the varying the metallicity (1/3 solar, and solar) and photoionizing radiation field (by scaling the Galactic ISM spectra component to 0, 1/10, 1/3, 3, and 10 of the original). The models with the combination of these parameters that acceptably reproduce the observed elemental abundance ratios indicate that the magnitude of the resulting correction varies within a couple of tenth of a dex from the value determined by the original model.

4.2.2 Dust Depletion

Dust depletion can severely affect the abundance measurements in DLAs and SDLAs (Pei, Fall, & Bechtold 1991, Pettini et al. 1997). Furthermore, it has been suggested that the dust depletion pattern in DLAs resembles sight-lines through the warm gas of the Galactic disk and halo (Lauroesch et al. 1996, Kulkarni, Fall, & Truran 1997). The study of depletion in QAL systems is very important and a necessary step in disentangling the nucleosynthetic signatures of the star formation associated with the system. In order to study the effects of dust on the abundances in the SDLA towards J2123−0050, I adopt the method of Vladilo (1998). For some of the commonly detected metals in DLAs and SDLAs (e.g., Zn, S, or N) the dust phase contribution to the total number density is negligible. By comparing the

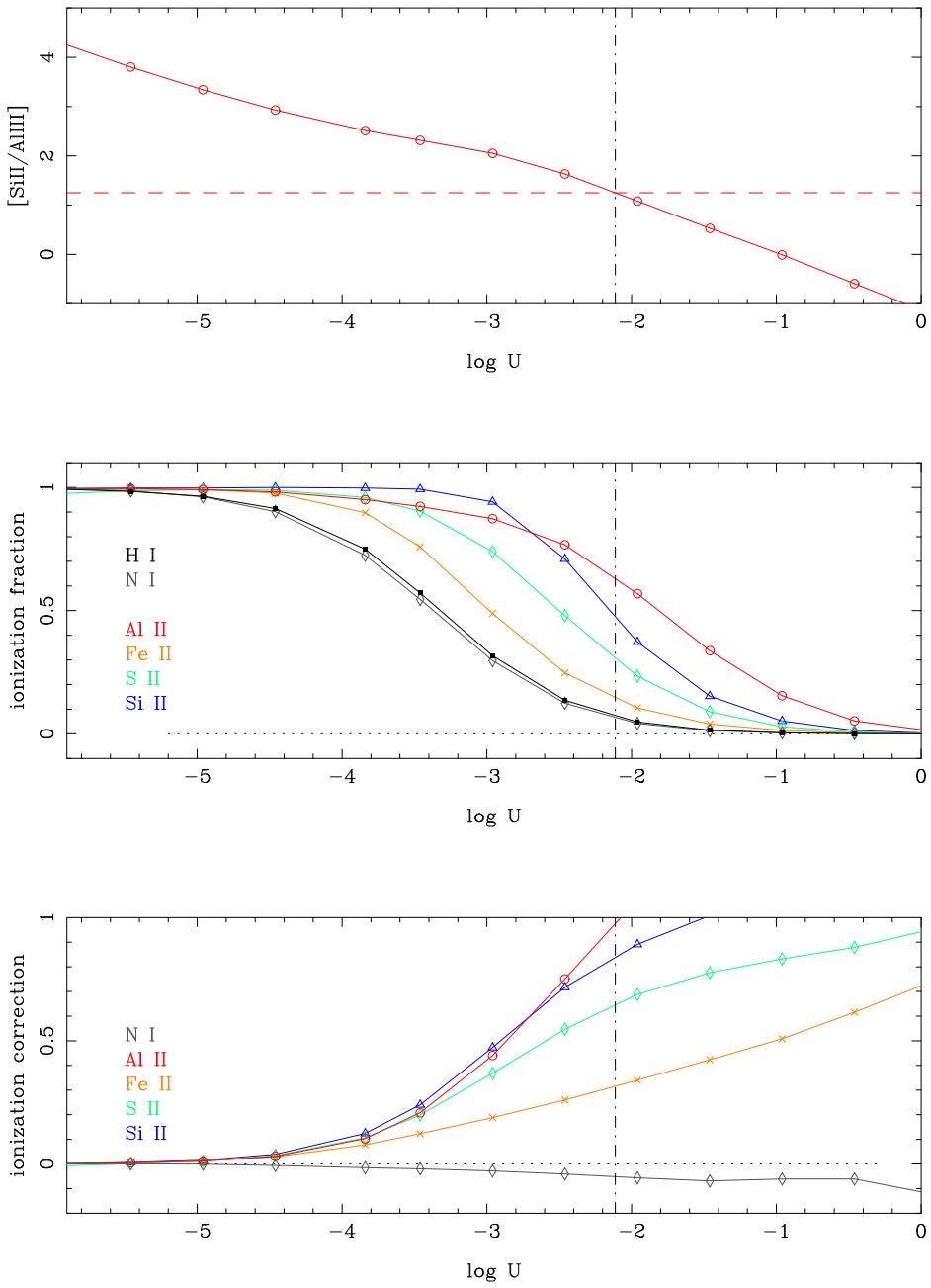

Figure 4.6: The top panel shows the predicted SiII to AlIII column density ratio from the CLOUDY models with the photoionizing spectrum containing both the average Galactic ISM and extragalactic HM spectra. The horizontal dashed lines are drawn at the measured ratio. The average ionization parameter inferred by comparing the observed values to the model has a value of −2.11. Predicted ionization corrections for the selected metal species from the same models are given in the lower panel.

abundance of a metal that condenses onto dust grains (X) to a metal that is not depleted (reference element Y), but is of similar nucleosynthetic origin, one can obtain the dust depletion correction in the following way. First, we define the dust-to-gas ratio relative to the Galactic value as:

$$\tilde{\kappa} = \frac{10^{[\mathrm{Y/H}]_{obs}} - 10^{[\mathrm{X/H}]_{obs}}}{f_{\mathrm{X},ISM} - f_{\mathrm{Y},ISM}}, \tag{4.4}$$

assuming Galactic type dust presented with Galactic dust fractions f_{ISM}, with values adopted from Savage & Sembach (1996). This enables one to calculate the corrected metallicity measured on the basis of element Y:

$$\tilde{Z}_{\mathrm{Y},corr} = [\mathrm{Y/H}]_{corr} = 10^{[\mathrm{Y/H}]_{obs}} + \tilde{\kappa} \times f_{\mathrm{Y},ISM}. \tag{4.5}$$

The dust depletion correction for an element X is then:

$$\delta_X = \log\left(1 - \frac{\tilde{\kappa}}{\tilde{Z}_{\mathrm{Y},corr}} 10^{-[\mathrm{X/Y}]_{obs}} f_{\mathrm{X},ISM}\right). \tag{4.6}$$

While iron and zinc are usually used for measurements of the dust-to-gas ratio, the spectrum of J2123−0050 does not cover any prominent zinc lines. However, the detection of S II and Si II gives an opportunity to probe the depletion of silicon. These two elements share similar nucleosynthetic origins, and sulphur is poorly depleted to dust, and as such is suitable for this study. Assuming an ISM dust fraction representative of the Galactic warm disk given by Savage & Sembach (1996) of $f_{\mathrm{Si},ISM} = 0.63$, and $f_{\mathrm{S},ISM} = 0.12$, I obtain a dust-to-gas ratio of $\tilde{\kappa} = 0.71$ from Equation 4.4 . The corrected metallicity of the system using the observed, ionization corrected abundance of sulphur is $\tilde{Z}_S \approx 0.64\ Z_{S_\odot}$, or [S/H]$\approx -0.20$. The dust depletion correction for silicon is $\delta_{\mathrm{Si}} = -0.61$, while for sulphur it is only $\delta_{\mathrm{S}} = -0.06$. This result falls in the locus of the values calculated by Vladilo (1998) for the warm Galactic disk depletion, and is higher than those typical of the Galactic halo. The total dust-to-gas ratio derived for the SDLA in J2123−0050 is substantially higher than any of the 17 DLAs studied in the sample of Vladilo

Table 4.1: Elemental abundances before and after ionization corrections

	log N(SiII) (cm^{-2})	log N(FeII) (cm^{-2})	log N(SII) (cm^{-2})	log N(NI)) (cm^{-2})	log N(AlIII) (cm^{-2})
Total	14.69±0.02	14.12±0.02	14.70±0.02	14.53±0.02	13.06 ± 0.01
$\log(X/H)_\odot$	−4.49	−4.55	−4.84	−4.22	-5.57 ± 0.02
$[X/H]_{raw}$	0.00	−0.51	+0.36	−0.43	−0.51
IC(X/H)	+0.80	+0.30	+0.62	−0.04	+0.62
δ(X/H)	−0.61	...	−0.06	...	...
$[X/H]_{corr}$	-0.19 ± 0.15	-0.81 ± 0.15	-0.20 ± 0.15	-0.39 ± 0.15	−1.17

(1998). However, the SDLA also has a substantially higher metallicity than the average by $\sim$ 1 dex, which might possibly account for the higher dust content.

4.2.3 Corrected Chemical Abundances

The derivation of ionization and dust depletion corrections allow for the calculation of corrected elemental abundances. Table 4.1 lists the measured metal ion column densities (see Chapter 2, § 2.3 for more details). The abundances values in the table are given relative to the reference to meteoric solar abundances $[X/H]_\odot$ of Grevesse, Asplund, & Sauval (2007) , except in the case of nitrogen for which the photospheric measurements are used because of the large discrepancy of meteoric to photospheric value.

The corrected abundances show sub-solar levels for all of the observed elements. Moreover, there is a large under-abundance of iron in comparison to the α-elements ([S/Fe]= 0.87). Relative enhancement of α-elements to iron may be a nucleosynthetic effect, because Fe is produced in longer lived low-mass stars, and is dispersed in the interstellar medium by SNe Type Ia. High [α/Fe] is a signature of SNe Type II enhancement, which disperses α-elements to ISM, before SNe Type Ia catch up.

Our J2123−0050 Keck/HIRES spectrum unfortunately does not offer the cov-

erage of zinc lines, which are required to calculate the dust depletion for iron. The true abundance of Fe is therefore likely to be considerably higher than the value quoted in Table 4.1. Vladilo (1998) finds the iron dust correction to be as high as -1.22 for models based on Galactic ISM type grains for systems with the Galactic halo-type metallicity and abundance ratios, and metal-to-dust ratio of 1 (slightly higher than $\tilde{\kappa}/\tilde{\mathrm{Z}}$ of SDLA towards J2123$-$0050 that has a value of ~ 0.86). It is therefore not possible to quantify precisely what the α enhancement might be in this absorber.

4.2.4 [N/α]

The use of nitrogen and α-element abundances in probing the star formation history of the high-end column density QAL systems is of particular interest. The main path for the nucleosynthesis of these two elements is the CN branch of the CNO cycle in which nitrogen is produced within the stellar H burning layer from oxygen and carbon. However, nitrogen has both a primary and secondary production component depending on whether ^{12}C and ^{16}O are fully produced during the helium burning by the star, or were condensed from the ISM when the star was formed. As a result, nitrogen produced in the secondary stage arises in higher metallicity environments where seed nuclei are already present in the ISM (Pettini et al. 2002, Henry & Prochaska 2003, Petitjean, Ledoux & Sruanand 2008, Pettini et al. 2008). The principal sources of primary N are thought to be intermediate mass stars (IMS) ($4 \leq \mathrm{M} \leq 7$ M$_\odot$) in their AGB phase. The effect of this hypothesis is that nitrogen lags behind oxygen in its release into the ISM (O is mostly produced by massive stars that become SNe Type II only tens of millions years after their formation). This time delay can be as long as 250 Myr (Henry & Prochaska 2003), and its effect can be seen in DLAs with measured nitrogen and oxygen, or sulphur (which is often used as a proxy for oxygen, because it is a typical α-element (Henry & Prochaska 2007, Pettini et al. 2008)). In fact, a surprisingly high fraction ($\sim$40%) of studied

DLAs in Pettini's sample did not attain the primary level of nitrogen production. The authors suggest that this is due to the low metallicity of the observed DLAs that preferentially selects young galaxies that have just condensed out of the IGM and started forming stars.

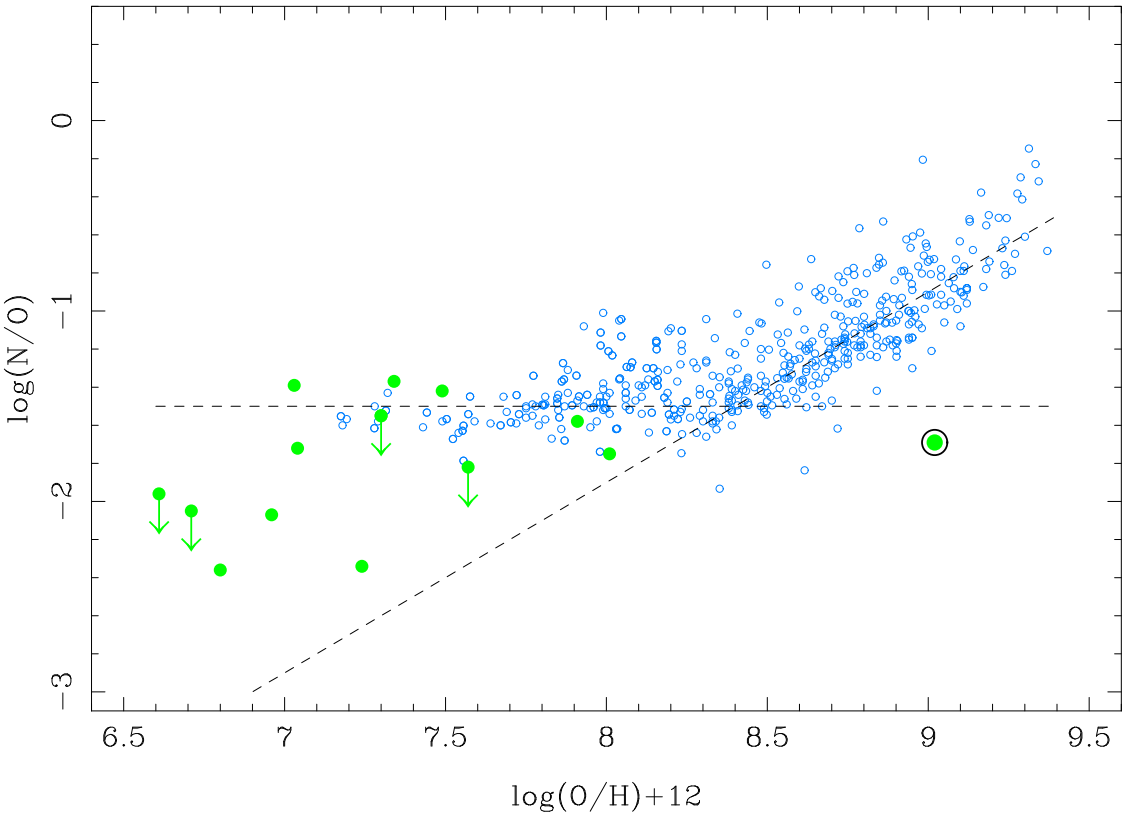

Figure 4.7: log(N/O) plotted against the system metallicity. SDLA in J2123−0050 (ringed green circle) is plotted against the DLA data (green circles) assembled from literature, and Galactic HII data (open blue circles) collected by Pettini et al. (2008).

Even though low metallicity systems have been studied extensively, there is a lack of measured N and O (or S) in higher metallicity systems. In order to examine the place of the SDLA towards J2123−0050 within the log(N/O) vs metallicity parameter space, I constructed Figure 4.7 using the abundance ratio of the SDLA compared to the data from extragalactic H II regions (from the sources assembled

by Pettini et al. 2008) and DLAs from literature. In the caases where measurement of oxygen was unavailable, I used sulphur, or silicon as a proxy, correcting $[X/H]_{sys}$ with $[X/O]_{\odot}$. From the unusual location of the SDLA in Figure 4.7 one could speculate that even at high metallicity the nitrogen comes from the primary production in these high-z systems. This could be true only if its origin does not hail necessarily from IMS. We return to the puzzle of the $[N/\alpha]$ ratio in this SDLA in Chapter 5.

4.2.5 C II*

Our knowledge of star formation and the properties of star forming environments in high redshift comes almost exclusively from the direct observation of starlight at high-z Lyman break galaxies, or reprocessed light through the dust emission in sub-mm galaxies (Wolfe et al. 2002). However, these extremely luminous objects are unlikely to be the progenitors of the majority of present day galaxies, but they might be precursors to the massive ellipticals which can be found in clusters at the present epoch (Wolfe et al. 2002). The support for this comes from a high comoving star formation rate, as well as the evidence for strong clustering (Adelberger et al. 1998). DLAs, on the other hand, may offer a more representative probe of the high redshift galaxy population. It is therefore of great interest to try to determine the star formation rates of DLAs.

Wolfe, Prochaska, & Gawiser (2003) derived a method to determine the properties of the star forming regions associated with the DLA sightlines through the use of the C II* λ1335 line. The method estimates [CII] 158μm emission from the strength of the C II* λ1335 absorption. Absorption resulting in the 1335 Å line arises from $^2P_{3/2}$, from which a 158 μm photon is spontaneously emitted during the decay to the $^2P_{1/2}$ fine-structure state in the ground $2s^22p$ term of C II. The [CII] 158μm is a principal coolant of interstellar neutral gas in the Galaxy (Wright et al. 1991). By assuming that cooling is dominated by the 158 μm line, the heating

rate Γ can be calculated by determining the [CII] cooling rate l_c. In the case of thermal equilibrium, heating equals cooling.

The emissivity of [CII] 158μm can be calculated from the column density of CII* λ1335 line following the expression of Pottasch, Wesselius, & van Duinen (1979):

$$l_c = \frac{N(\mathrm{C\,II^*})h\nu_{ul}A_{ul}}{N(\mathrm{H\,I})}\ ergss^{-1}Hz^{-1}, \tag{4.7}$$

where A_{ul} is the Einstein coefficient, and $h\nu_{ul}$ is the energy of the 158μm transition. Taking the J2123−0050 values for N(HI) and N(CII*) I infer the value of $1.2 \times\ 10^{-25}$ ergs s^{-1} Hz^{-1}. When plotted against the hydrogen column density and compared with the DLAs (Figure 4.8), and the average Galactic ISM adopted from the study of Wolfe, Prochaska, & Gawiser (2003), the SDLA occupies an unusual location, with the cooling rate higher than that of both the averaged ISM in Galactic disk, and all DLA measurements to date.

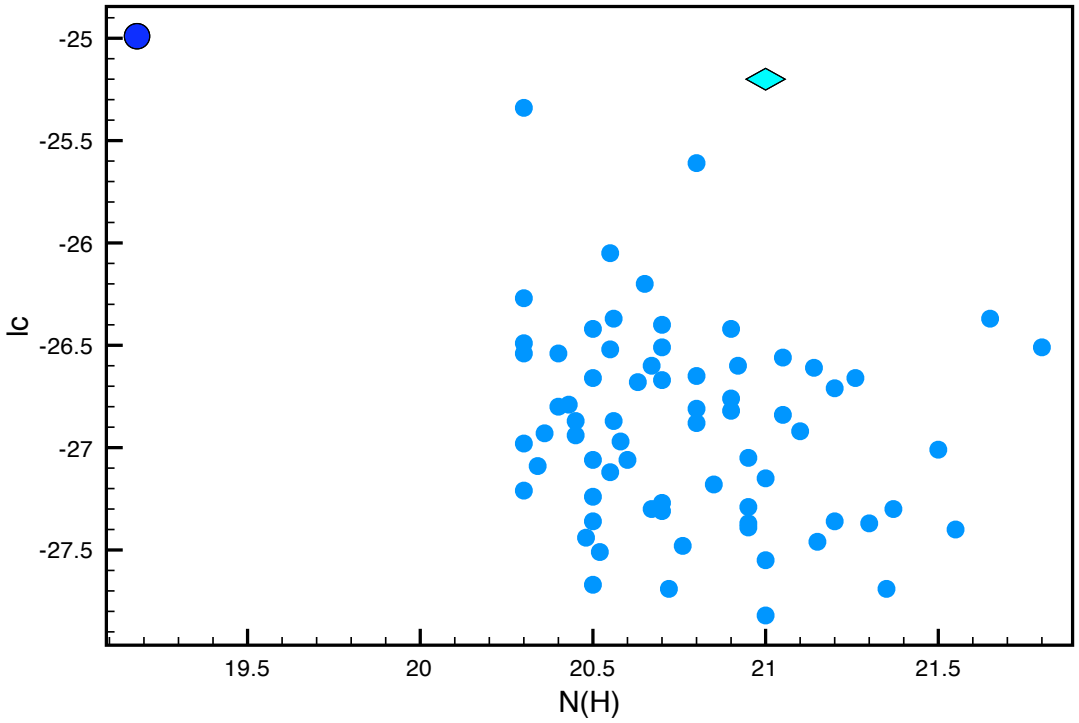

Figure 4.8: 158μm line cooling rate in SDLA in J2123−0050 ploted against the average Galactic (light blue diamond point) and DLA measurements (blue filled circles). Plot adapted from the study of Wolfe, Prochaska, & Gawiser (2003). The gap in points bellow log$N$(H I) $\approx$ 20.3 is due to the selection criterion in the sample of (Wolfe et al. 2008).

Chapter 5 | *Discussion*

In this thesis I presented a study of the extraordinary case of the SDLA towards the quasar J2123−0050. This sightline offers a unique opportunity to study the high redshift ISM. Here I give a brief summary, discuss my findings, and point out the possible importance of this study for our general understanding of DLAs and SDLAs.

The SDLA towards J2123−0050 is a kinematically complex system with at least 15 metal absorption components spread over 400 $\mathrm{km\,s^{-1}}$ in velocity space. The kinematic structure has two distinct velocity complexes, a main complex centred at a redshift of $z = 2.0593$, and a satellite complex centred at $z = 2.0568$ (offset by about 230 $\mathrm{km\,s^{-1}}$ from the main complex redshift). The satellite complex harbors the absorption from ionized metal species along with the neutral hydrogen, while the main complex additionally gives rise to neutral and fine-structure metal absorption and molecular absorption.

I performed column density measurements of neutral hydrogen (HI), molecular hydrogen (H_2 and HD), and some metal species using curve of growth and Voigt profile fitting methods. The total column density of neutral hydrogen obtained through the Voigt fit to the damped Lyα profile is $N(\mathrm{HI}) = 10^{19.25\pm0.2}\mathrm{cm^{-2}}$. This N(HI) places this system in the SDLA sub-class of Lyman limit systems. The column densities of the main and satellite complexes are respectively $N(\mathrm{HI})_{main} = 10^{19.18\pm0.15}$ $\mathrm{cm^{-2}}$, and $N(\mathrm{HI})_{sat} = 10^{18.40\pm0.30}$ $\mathrm{cm^{-2}}$. The two-component fit to the H_2 molecular absorption gives a molecular hydrogen fraction of $\log f(H_2) = -2.56$, while the abundance of deuterated hydrogen molecule $\log(N(\mathrm{HD}/2N(H_2))$ is -2.75. The metallicity inferred from the raw abundance of singly ionized sulphur is

[S II/H I] = +0.36. The relative raw abundance of sulphur to iron of [S II/Fe II] = 0.85 is suggestive of an α-element enhancement.

These measurements place the SDLA J2123−0050 system among the highest metallicity QAL systems, and give a rise to a number of unexpected results:

1. Even though the age of the universe at the epoch of the system was only about 3.2 Gyr, the gas in this SDLA has achieved a super–solar metallicity level ([S II/H I] = +0.36). For comparison, the average metallicity of a DLA at this high redshift is only [M/H]~ -1.2 (Wolfe, Gawiser, & Prochaska 2005).

2. The [N/α] ratio is surprisingly low for such a high metallicity. Nitrogen production is characterized by primary and secondary production curves. The raw measurements place this system in a location under both the curves. At such a high metallicity it is expected that C and O seeds should already be in place in the star–forming gas, and the [N/α] level should at least surpass that of the primary production level.

3. The [CII] 158 μm line is a primary coolant of the neutral ISM. The [CII] 158 μm line cooling rate can be measured in this system through C II* λ1335Å, yielding a value of $l_c = 1.2 \times\ 10^{-25}$ ergs s^{-1} cm^{-2}. Comparing to the cooling rates of DLAs from the sample of Wolfe, Prochaska, & Gawiser (2003) the SDLA towards J2123−00 has the highest value. This is not expected because absorbers with higher neutral hydrogen column density than the SDLA towards J2123−0050 would contain more neutral gas and hence have a higher cooling efficiency.

4. Compared to local sightlines, the system has an unusually high molecular fraction for its relatively low neutral hydrogen column density. However, the H_2 excitation temperatures in the system are similar to those in local sightlines, suggesting that the physical properties of the gas lie in the range spanned by Galactic and Magellanic Cloud gas.

5. The system hosts the third HD molecular detection in QALs. Furthermore, the SDLA towards J2123−0050 has the lowest N(H I) of the three systems in which HD is detected, and the highest $\log(N(\mathrm{HD})/2N(\mathrm{H_2}))= -2.75$. For comparison, in the *FUSE* Galactic ISM sample of Lacour et al. (2005), the sightlines with similar neutral column density exhibit $\log(N(\mathrm{HD})/2N(\mathrm{H_2}))\sim-5.8$, while the primordial (D/H) level is −4.59 (Komatsu et al. 2009).

To investigate some of these discrepancies I perform a study of the effects of ionization and dust depletion on the abundance measurements to assess whether they are responsible for the unusual properties of this SDLA.

The SDLA in J2123−0050 is a multi-phase system, as suggested by the b-parameters of neutral and singly ionized lines of sulphur, and the presence of the strong lines of ionized metal species (e.g., Al III, Si III, Si IV and C IV). Because of the kinematic complexity and self-blending it is not possible to disentangle the contribution of separate phases to the total neutral hydrogen column density. This can be circumvented by modeling this system as a single-phase cloud. Traditionally, DLAs and SDLAs are modeled as single-phase clouds because of the simplicity of such a model. I adopt the same strategy, but also examine the bias that such an assumption introduces in the final results.

I performed a theoretical experiment using CLOUDY that first produces a mock two-phase absorber, and then tries to reproduce the two-phase cloud abundances from a single-cloud model ionization correction. The experiment shows that the abundances can never be fully recovered, and the corrections are an order of magnitude higher than the usual errors of measuring column densities in QALs. However, for the examined radiation field and metallicity range, the error in reproducing the abundances once corrections are applied is relatively small, on the order of a couple of tenths of a dex. Furthermore, the ionization parameter of the "warm" gas is recovered to within 0.1 dex. This result legitimizes the use of single-phase photoionization modeling in deriving the ionization correction.

After assessing the biases of the single-cloud modeling approach, I model the ionization properties of the system towards J2123−0050 using the photoionization code CLOUDY. In the model, I assumed the photoionizing source to be a mix of the Haardt & Madau extragalactic background spectrum and the average Galactic ISM spectrum. I stopped the calculations when the model reached the measured column density of neutral hydrogen. The inferred ionization fraction of the phase that gives rise to singly ionized metal species obtained in this fashion is $\chi \approx 93\%$. If we assume that the bulk of the neutral hydrogen comes from this phase, then the total hydrogen column density is $10^{20.3}$ cm^{-2} (the error on this estimate due to the modeling is on the order of 0.2 dex). The gas phase which gives rise to neutral metal lines, and possibly molecular absorption, is omitted from this calculation and might contribute to the total number density of hydrogen. Nonetheless, the column density ratio of the neutral to the single metal species ($\log(N(\mathrm{S\,I})/N(\mathrm{S\,II})) = -2.81$) suggests that the ionized phase dominates the total metal and hydrogen number density budget.

I also performed calculations of dust depletion following the prescription of Vladilo (1998). For the SDLA towards J2123−0050 the dust depletion corrections are available only for the α-elements because the Zn lines are not covered in our Keck/HIRES spectra.

When the ionization and dust corrections are applied to the raw measurements, the changes in the results are reflected in correcting the discrepancies discussed above in the following manner:

1. Corrected for ionization and dust, the metallicity of the system is [S/H]= −0.20. This is a 0.56 dex correction compared to the raw abundance measurement (for reference check Table 4.1 in Chapter 4) The α-elements still seem to be enriched relative to iron, but depending on the level of dust correction for Fe, this enrichment could be negligible. Vladilo (1998) found the dust corrections for iron can be as high as 1.2 dex. It is therefore not possible

to quantify the level of α-enhancement in this system. Nonetheless, the metallicity of the system places this SDLA among the small subset of metal-rich absorbers at z$\approx$2.

2. Since NI has an ionization potential similar to HI, the ionization correction for this element is negligible. It is also not expected that this element depletes much onto dust grains in sightlines that pass through diffuse gas (Meyer, Cardelli, & Sofia 1997). The α-elements detected in the SDLA (sulphur, and silicon), on the other hand, need to be corrected for both dust and ionization. The corrected abundances are presented on the Figure 5.1. The magnitude of the corrections place the system in the locus of sightlines that we observe in the local universe in the N/α vs. α/H plane at an intermediate position between primary and secondary production levels.

3. To calculate the cooling rate of [CII]158 μm, Pottasch, Wesselius, & van Duinen (1974) use the fact that Galactic sightlines are neutral so that the HI column density approximates the total column density of the sightline. If the HI column density $N(\mathrm{HI}) = 10^{19.18}$ cm^{-2} in Equation 2.7, Chapter 2 is replaced with total column density of $N(\mathrm{H}) = 10^{20.3}$ cm^{-2} (i.e., the value calculated after the ionization corrections are applied) the cooling rate takes a value of 8.7×10^{-26} ergs s^{-1} Hz^{-1}. The magnitude of this correction (presented in Figure 5.2) places the system among the values measured from DLAs with similar column density in the sample of Wolfe et al. (2008).

4. The molecular fraction of the system is recalculated using the total column density of hydrogen derived through the photoionization modelling, leading to a value of log $f(\mathrm{H_2}) = -3.87$ (see Figure 5.3). This result places the system among the grids of $\mathrm{H_2}$ models with gas properties similar to that of Galactic sightlines, and agrees with the result of the $\mathrm{H_2}$ excitation temperature analysis. However, the molecular gas is not produced in the ionized phase

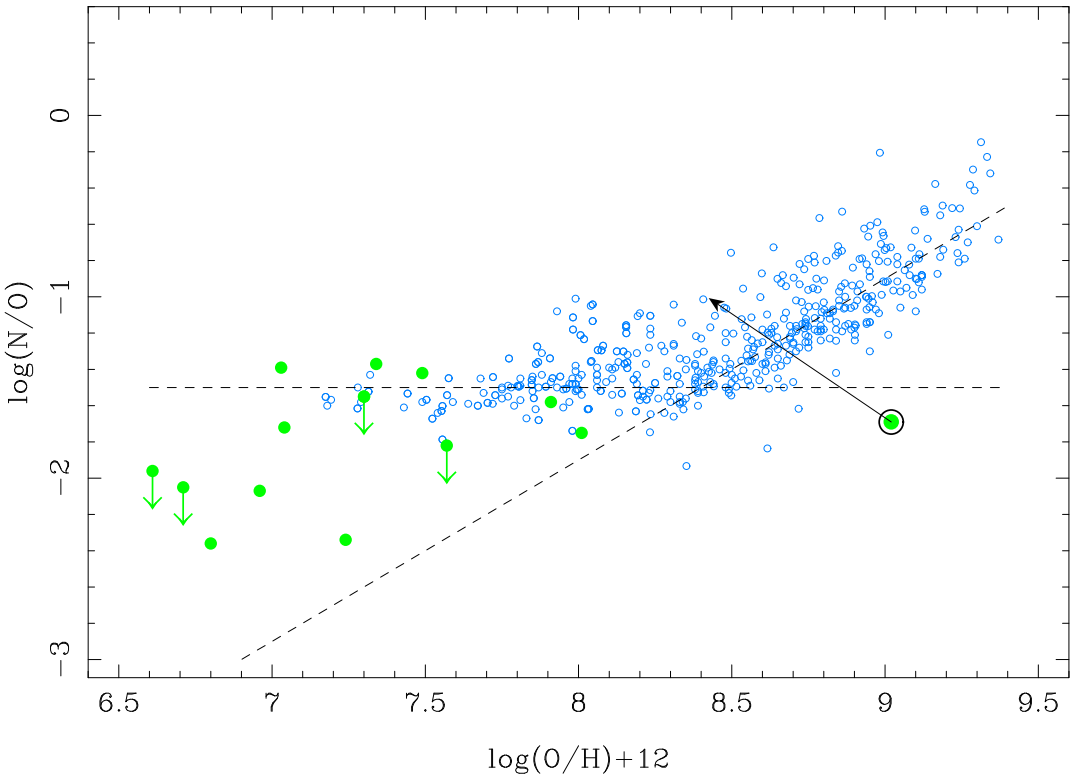

Figure 5.1: log(N/O) ratio plotted against the system metallicity log(O/H)+12. Silicon and sulfur abundance is used as a proxy for the systems that lack O measurement (corrected with solar log(X/O)). SDLA in J2123−0050 (ringed green circle) is plotted against the DLA data (green circles) from literature and Galactic HII sightlines (open blue circles) assembled by Pettini et al. (2008). The arrow points to the J2123-0050 ratio corrected for the ionization and dust depletion.

because its temperature (few thousand K) is too high for H_2 to be present, so the question arises of the validity of applying this correction when calculating molecular fraction. The sightlines through the Galaxy and the Magellanic Clouds, which are used for the comparison, sample the gas that is mostly neutral even though the density of the gas along the sightline can vary. The total column density of these diffuse clouds is therefore a sum of all the gas in the neutral phase and the denser clumps that give rise to the molecular absorption. However, the SDLA towards J2123−0050 is mostly ionized. If the

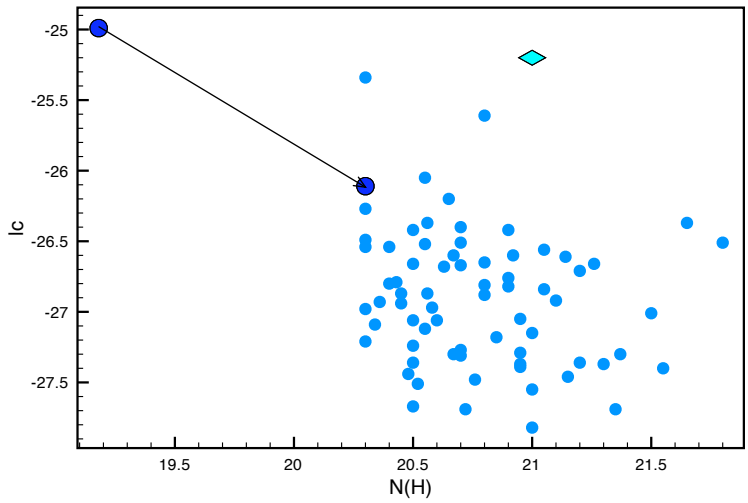

Figure 5.2: The 158μm line cooling rate in the SDLA towards J2123−0050 plotted against the average Galactic (light blue diamond point), and DLA measurements (blue filled circles) of Wolfe et al. (2008). The gap in the points distribution below log$N$(H I) $\approx$ 20.3 is due to the selection criterion in the sample of Wolfe et al. (2008). Corrected for ionization (the arrow marks the direction and the extent of the correction), the cooling rate in the SDLA towards J2123−0050 falls in the locus occupied by DLA systems at high redshift.

high-z ISM observed in J2123−0050 is physically similar to the local one, it is possible that the radiation from a nearby star formation region ionized the lower density gas, while the molecular gas was preserved in colder, and denser clumps. This scenario motivates the application of the ionization correction to the H_2 fraction measurement.

Although the corrected properties of this SDLA make it similar to the Galaxy in a number of ways, the corrections can not explain the high HD fraction. Galactic HD fractions measured in the *FUSE* survey of Snow et al. (2008) range from −6.18 to −5.13, compared to −2.75 for the SDLA towards J2123−0050. However, the HD fraction should not be used as a reliable deuteration diagnostic for the diffuse

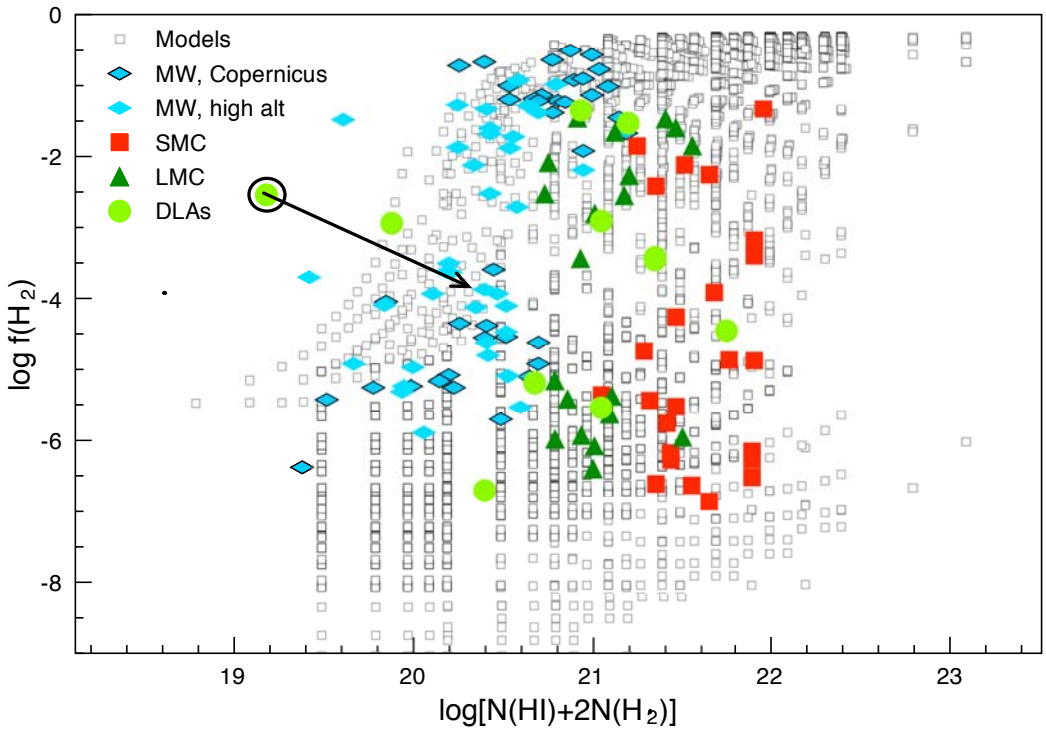

Figure 5.3: The QAL systems, Galactic, and Magellanic Cloud sightlines molecular fraction compared to the model grids. The arrow gives an extent and the direction of the correction when ionized hydrogen is included in the total hydrogen budget when calculating $f(\mathrm{H_2})$.

sightlines (Lacour et al. 2005). This is because the HD fraction depends on the grain composition, size and temperature, and this is poorly understood for a diffuse medium. However, the theoretical models of Cazaux et al. (2008), albeit for a lower metallicity than the SDLA studied here, show that for smaller size grains and higher grain temperatures ($T_{grain} > 150$ K), the efficiency of HD formation can be enhanced in comparison to $\mathrm{H_2}$. An alternative explanation for an apparently high deuterium fraction, might be that the local radiation has photo-evaporated and destroyed some of the $\mathrm{H_2}$ molecules, because the smaller evaporation energy is needed for $\mathrm{H_2}$ comparing to its deuterated counterparts. Furthermore, $(N(\mathrm{HD})/2N(\mathrm{H_2}))$ can be

taken as a measurement of the galactic D/H ratio only if the gas in the system is predominately in the molecular form (for both hydrogen and deuterium), which is true only in the case of dense molecular cloud cores.

In summary, the magnitude of the ionization corrections has a profound impact on the interpretation of this SDLA. The correction raises the total hydrogen column density of the system, and lowers the metallicity and the abundances of all the elements covered. Such corrections can resolve the discrepancies between the theoretical expectations and the raw observations. After applying the corrections to the SDLA towards J2123−0050 the results are suggestive of an ISM that exhibits properties similar to those of the gas found in local sightlines through the Galaxy.

The careful consideration of the single-cloud modelling strategy presented in Chapter 4 implies that, when a multiphase medium is approximated by a single-phase model, the corrected hydrogen and metal species column densities tend to be overestimated. However, the errors introduced by such an approach are significantly smaller than the ionization corrections themselves (which can be as high as 0.7 dex). The application of ionization corrections is therefore a necessary step in deriving the abundances of low column density systems. It is also worth noting that the iron abundance is recovered better than the silicon abundance (see Figures 4.4 & 4.5). An error induced by the single-cloud modelling approach can therefore significantly alter the interpretation of the relative metal abundances found in the system by diluting the signature of nucleosynthetic origins, such as an α-enhancement, making the abundance analysis of SDLAs a difficult task.

Bibliography

Abgrall H., Roueff E., Drira I.,2000, A&AS, 141, 297

Adelberger K. L., Steidel C. C., Giavalisco M., Dickinson M., Pettini M., Kellogg M., 1998, ApJ, 505, 18

Bahcall J. N., Salpeter E. E., 1965, ApJ, 142, 1677

Beasley M. A., Brodie J. P., Strader J., Forbes D. A., Proctor R. N., Barmby P., Huchra J. P., 2005, AJ, 129, 1412

Black J. H., 1987, ASSL, 134, 731

Bond J. R., Kofman L., Pogosyan D., 1996, Natur, 380, 603

Bouché N., Murphy M. T., Péroux C., Csabai I., Wild V., 2007, NewAR, 51, 131

Browning M. K., Tumlinson J., Shull J. M., 2003, ApJ, 582, 810

Carswell, R. F., Webb, J. K., Cooke, A. J., & Irwin, M. J. 1996, Voigt Profile Fitting Program (VPFIT)

Cazaux S., Caselli P., Cobut V., Le Bourlot J., 2008, A&A, 483, 495

Condon, J. J., Cotton, W. D., Greisen, E. W., Yin, Q. F., Perley, R. A., Taylor, G. B., & Broderick, J. J. 1998, AJ, 115, 1693

Cowie L. L., Songaila A., Kim T.-S., Hu E. M., 1995, AJ, 109, 1522

Charlton J. C., Narayanan A., Ding J., 2003, AAS, 35, 1250

Churchill, C. W 2009, QSO Absorption Line Book, in prep

D'Odorico V., Petitjean P., 2001, A&A, 370, 729

Dessauges-Zavadsky M., Péroux C., Kim T.-S., D'Odorico S., McMahon R. G., 2003, MNRAS, 345, 447

Dessauges-Zavadsky M., Ellison S. L., Murphy M. T., 2009, MNRAS, 396, L61

Draine B. T., 1978, ApJS, 36, 595

Ferland G. J., Korista K. T., Verner D. A., Ferguson J. W., Kingdon J. B., Verner E. M., 1998, PASP, 110, 761

Ferrara A., Scannapieco E., Bergeron J., 2005, ApJ, 634, L37

Field G. B., Somerville W. B., Dressler K., 1966, ARA&A, 4, 207

Field G. B., Goldsmith D. W., Habing H. J., 1969, ApJ, 155, L149

Haardt F., Madau P., 1996, ApJ, 461, 20

Hartmann J., 1904, ApJ, 19, 268

Hawking S. W., 1982, PhLB, 115, 295

Herbert-Fort S., Prochaska J. X., Dessauges-Zavadsky M., Ellison S. L., Howk J. C., Wolfe A. M., Prochter G. E., 2006, PASP, 118, 1077

Henry R. B. C., Prochaska J. X., 2003, ASPC, 304, 396

Henry R. B. C., Prochaska J. X., 2007, PASP, 119, 962

Herzberg G., 1950, msms.book

Holland W. S., et al., 1999, MNRAS, 303, 659

Hoyle F., Ellis G. R. A., 1963, AuJPh, 16, 1

Howk J. C., Sembach K. R., 1999, ApJ, 523, L141

Grevesse N., Asplund M., Sauval A. J., 2007, SSRv, 130, 105

Gunn J. E., Peterson B. A., 1965, ApJ, 142, 1633

Ivanov T. I., Roudjane M., Vieitez M. O., de Lange C. A., Tchang-Brillet W.-Ü. L., Ubachs W., 2008, PhRvL, 100, 093007

Izotov Y. I., Schaerer D., Charbonnel C., 2001, ApJ, 549, 878

Jenkins E. B., Meloy D. A., 1974, ApJ, 193, L121

Jura M., 1975, ApJ, 197, 581

Jura M., 1975, ApJ, 197, 575

Jura M., 1974, ApJ, 191, 375

Komatsu E., et al., 2009, ApJS, 180, 330

Kulkarni V. P., Fall S. M., Truran J. W., 1997, ApJ, 484, L7

Kurucz R. L., 1991, BAAS, 23, 1047

Lacour S., et al., 2005, A&A, 430, 967

Lauroesch J. T., Truran J. W., Welty D. E., York D. G., 1996, PASP, 108, 641

Lanzetta K. M., McMahon R. G., Wolfe A. M., Turnshek D. A., Hazard C., Lu L., 1991, ApJS, 77, 1

Lanzetta K. M., Bowen D. V., Tytler D., Webb J. K., 1995, ApJ, 442, 538

Ledoux C., Petitjean P., Srianand R., 2003, MNRAS, 346, 209

Lu L., Sargent W. L. W., Barlow T. A., 1996, ASPC, 99, 105

Madau P., 2007, arXiv, arXiv:0706.0123

McKee C. F., Ostriker J. P., 1977, ApJ, 218, 148

McKee C. F., 1995, ASPC, 80, 292

Meyer D. M., Cardelli J. A., Sofia U. J., 1997, ApJ, 490, L103

Milutinović N., Rigby J. R., Masiero J. R., Lynch R. S., Palma C., Charlton J. C., 2006, ApJ, 641, 190

Molaro P., Bonifacio P., Centurión M., D'Odorico S., Vladilo G., Santin P., Di Marcantonio P., 2000, ApJ, 541, 54

Narayanan A., Charlton J. C., Masiero J. R., Lynch R., 2005, ApJ, 632, 92

Narayanan A., Misawa T., Charlton J. C., Ganguly R., 2006, AJ, 132, 2099

Narayanan A., Charlton J. C., Misawa T., Green R. E., Kim T.-S., 2008, ApJ, 689, 782

Noterdaeme P., Ledoux C., Petitjean P., Srianand R., 2008, A&A, 481, 327

Noterdaeme P., Petitjean P., Ledoux C., Srianand R., Ivanchik A., 2008, A&A, 491, 397

Pei Y. C., Fall S. M., Bechtold J., 1991, ApJ, 378, 6

Péroux C., McMahon R. G., Storrie-Lombardi L. J., Irwin M. J., 2003, MNRAS, 346, 1103

Péroux C., Dessauges-Zavadsky M., D'Odorico S., Kim T.-S., McMahon R. G., 2003, MNRAS, 345, 480

Péroux C., Dessauges-Zavadsky M., D'Odorico S., Kim T.-S., McMahon R. G., 2007, MNRAS, 382, 17

Petitjean P., Ledoux C., Srianand R., 2008, A&A, 480, 349

Petitjean P., Ledoux C., Noterdaeme P., Srianand R., 2006, A&A, 456, L9

Pettini M., Ellison S. L., Steidel C. C., Bowen D. V., 1999, ApJ, 510, 576

Pettini M., Ellison S. L., Bergeron J., Petitjean P., 2002, A&A, 391, 21

Pettini M., Zych B. J., Steidel C. C., Chaffee F. H., 2008, MNRAS, 385, 2011

Pettini M., King D. L., Smith L. J., Hunstead R. W., 1997, ApJ, 478, 536

Pottasch S. R., Wesselius P. R., van Duinen R. J., 1979, A&A, 74, L15

Prochaska J. X., Howk J. C., O'Meara J. M., Tytler D., Wolfe A. M., Kirkman D., Lubin D., Suzuki N., 2002, ApJ, 571, 693

Prochaska J. X., Wolfe A. M., 1999, ApJS, 121, 369

Prochaska J. X., 2006, ApJ, 650, 272

Reynolds R. J., Magee K., Roesler F. L., Scherb F., Harlander J., 1986, ApJ, 309, L9

Reynolds R. J., Haffner L. M., Tufte S. L., 1999, ASPC, 168, 149

Sandage A., 1965, ApJ, 141, 1560

Sargent W. L. W., 1980, PhyS, 21, 753

Savage B. D., Sembach K. R., 1996, ApJ, 470, 893

Sivan J. P., 1974, A&AS, 16, 163

Slavin J. D., Shull J. M., Begelman M. C., 1993, ApJ, 407, 83

Shull J. M., Beckwith S., 1982, ARA&A, 20, 163

Snow T. P., Ross T. L., Destree J. D., Drosback M. M., Jensen A. G., Rachford B. L., Sonnentrucker P., Ferlet R., 2008, ApJ, 688, 1124

Spitzer L. J., 1956, ApJ, 124, 20

Springel, V. et al., 2005, Natur, 435, 629

Springel V., Frenk C. S., White S. D. M., 2006, Natur, 440, 1137

Srianand R., Noterdaeme P., Ledoux C., Petitjean P., 2008, A&A, 482, L39

Storrie-Lombardi L. J., Wolfe A. M., 2000, ApJ, 543, 552

Tripp T. M., Sembach K. R., Bowen D. V., Savage B. D., Jenkins E. B., Lehner N., Richter P., 2008, ApJS, 177, 39

Trumpler R. J., 1930, PASP, 42, 267

Tumlinson J., et al., 2002, ApJ, 566, 857

Tumlinson J., 2006, ASPC, 348, 401

Varshalovich D. A., Ivanchik A. V., Petitjean P., Srianand R., Ledoux C., 2001, AstL, 27, 683

Vladilo G., 1998, ApJ, 493, 583

Vladilo G., Centurión M., Bonifacio P., Howk J. C., 2001, ApJ, 557, 1007

Vogt S. S., et al., 1994, Proc. SPIE, 2198, 362

Weymann R. J., Carswell R. F., Smith M. G., 1981, ARA&A, 19, 41

Wolfe, A. M., Turnshek, D. A., Smith, H. E., & Cohen, R. D. 1986, ApJSS, 61, 249

Wolfe A. M., Prochaska J. X., Gawiser E., 2003, ApJ, 593, 215

Wolfe A. M., Gawiser E., Prochaska J. X., 2005, ARA&A, 43, 861

Wolfe A. M., Prochaska J. X., Jorgenson R. A., Rafelski M., 2008, ApJ, 681, 881

Wright E. L., 1991, ApJ, 375, 608

York D. G., 1974, ApJ, 193, L127